IN-02

163210

P68

NASA Technical Memorandum 4420

Development of a Large-Scale, Outdoor, Ground-Based Test Capability for Evaluating the Effect of Rain on Airfoil Lift

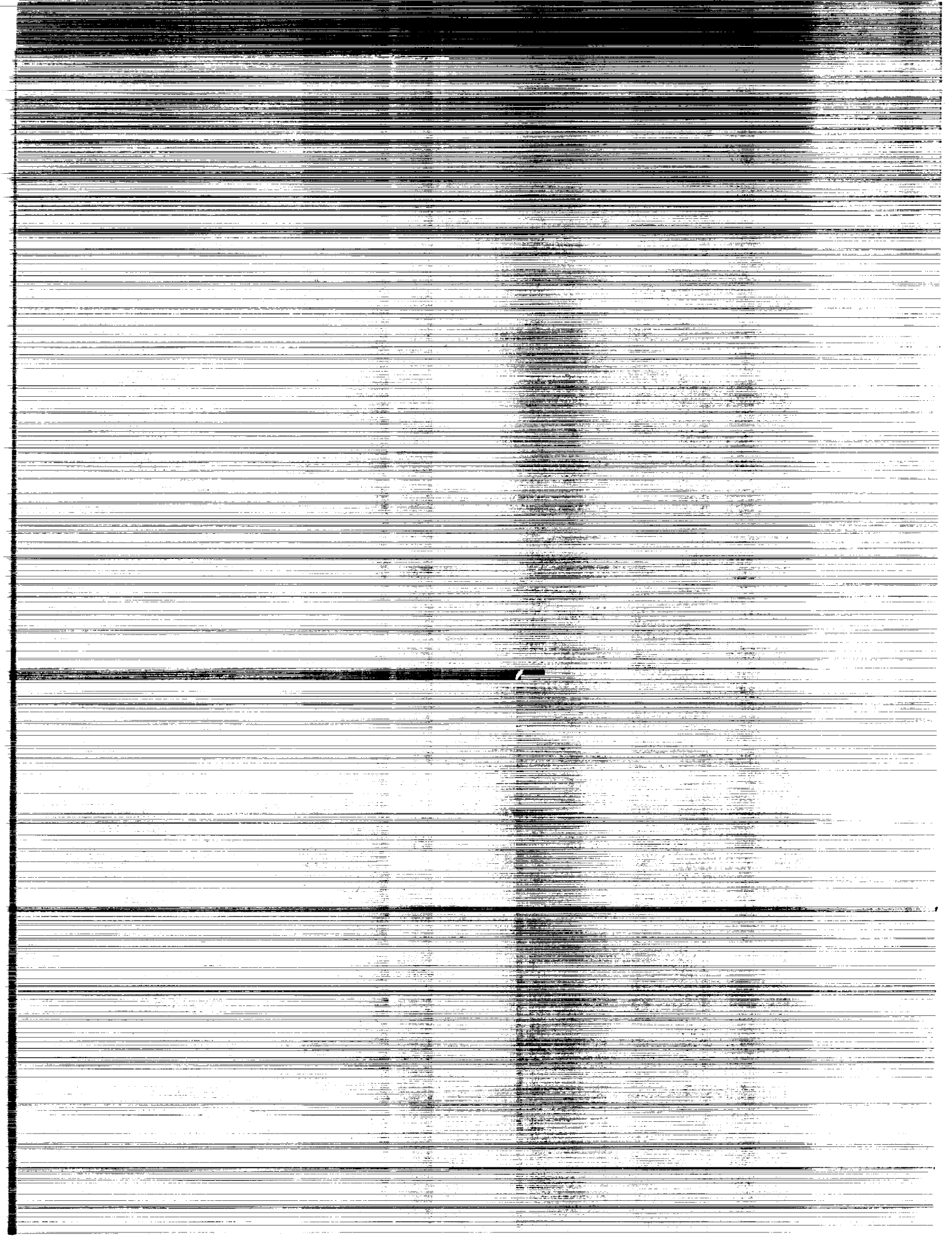Gaudy M. Bezos and Bryan A. Campbell

APRIL 1993

NASA

NASA Technical Memorandum 4420

Development of a Large-Scale, Outdoor, Ground-Based Test Capability for Evaluating the Effect of Rain on Airfoil Lift

Gaudy M. Bezos and Bryan A. Campbell
Langley Research Center
Hampton, Virginia

Summary

A large-scale, outdoor, ground-based test capability for acquiring aerodynamic data in a simulated rain environment was developed at the Langley Aircraft Landing Dynamics Facility (ALDF) to assess the effect of rain on airfoil performance. The ALDF test carriage was modified to transport a wing, mounted between circular endplates, along a 3000-ft track at full-scale aircraft approach speeds. The wing had an NACA 64-210 airfoil section and was equipped with leading-edge and trailing-edge high-lift devices deployed to simulate landing conditions. The wing was of rectangular planform and had a 10-ft chord and 13.1-ft span. The airfoil section chosen was representative of cambered, commercial transport wings and ensured the consistency between the existing rain effects wind tunnel data base and the ALDF test. An overhead rain simulation system was constructed along a 525-ft section of the track. The ALDF rain simulation system produced realistic rainfall intensities of 2, 10, 30, and 40 in/hr that were consistent with airborne and ground-based rainfall data measured in convective rainstorms. Aerodynamic data were acquired with and without the rain simulation system turned on. The facility carriage speed ranged from 100 to 170 knots. The wing angle of attack, which could be changed between test runs, ranged from 7.5° to 19.5° in 2° increments.

The methodology used to design, calibrate, and operate the ALDF rain simulation system is described in detail. The data acquisition and reduction processes are presented along with sample force data illustrating the environmental effects on data accuracy and repeatability for the "rain-off" test condition. Wind limits were placed on the operation of the rain simulation system and the acquisition of aerodynamic data to ensure quality aerodynamic measurements. Data are also presented on the raindrop-size distribution, rain field uniformity, and rainfall intensity obtained during the calibration of the ALDF rain simulation system.

Introduction

Since 1971, research has been ongoing to determine the nature and characteristics of the wind shear phenomenon. Low-altitude wind shear/microburst phenomena have long been recognized as a hazard to aircraft landing and takeoff operations. In 1977, the Federal Aviation Administration (FAA) conducted a study on aircraft accidents and incidents (1964–1976) in which low-altitude wind shear could have been a contributing factor (ref. 1). The study, which identified 25 cases (23 approach or landing and 2 takeoff) involving large aircraft (in excess of 12 500 lb), indicated that 10 cases had occurred in a rain environment, 5 of which were classified as intense thunderstorm-type rain encounters. These findings led to the reconsideration of rain associated with convective storms as being a potential weather-related aircraft safety hazard.

Rain associated with convective thunderstorms has been of interest to the meteorological and aviation communities for many years. The parameters used to characterize rain are the rainfall rate and the liquid water content. At ground level the rainfall rate, which is the rate at which rain falls (usually expressed in either in/hr or mm/hr), is generally used to characterize a rain event. For airborne measurements, the relevant parameter is the liquid water content, which is the mass of liquid water contained in a unit volume of air (usually expressed in grams per cubic meter (g/m^3) of air). The relationship between liquid water content and rainfall rate is uniquely dependent on the type and intensity level of the storm as detailed in references 2 and 3. Airborne measurements by Roys and Kessler (ref. 4) and ground-based measurements by Melson (ref. 5) identified the existence of localized regions of high-intensity rainfall in convective thunderstorms. Values of in-cloud liquid water content averaging $8.4 \ g/m^3$ with a peak value of $44 \ g/m^3$ were measured with an instrumented F-100 airplane in reference 4. Over 7000 rain events were measured at ground level with rates above 4 in/hr, with a maximum rain event of 29 in/hr in reference 5.

Prior to the start of the present research program, the earliest analytical work on the effect of rain on aircraft performance was conducted by Rhode in 1941 (ref. 6). His analysis indicated that drag increases associated with the momentum imparted to a McDonnell Douglas DC-3 aircraft encountering a rain cloud with a liquid water content of $50 \ g/m^3$ (approximately 64 in/hr) would cause an 18-percent reduction in airspeed. Rhode considered such an encounter to be of little consequence to an aircraft flying at 5000 ft. Because low-visibility takeoffs and landings were not routine in 1941, the consequences of a high-intensity (or "heavy") rain encounter during these phases of flight were not considered. However, for a modern-day transport aircraft, such an airspeed loss during takeoff or landing would be significant.

In 1977, NASA spearheaded the development of a broad experimental and analytical research effort to determine the effect of heavy rain on aircraft performance. The experimental research program at the Langley Research Center was initiated by the findings of the Haines and Luers study (ref. 7). In 1979 Haines and Luers, under contract from the

NASA Wallops Flight Facility, were tasked to analytically evaluate the effect of heavy rain on aircraft landing performance. Their study refined the work of Rhode by estimating the effect of rain on a modern-day transport. Their analysis indicated that a large transport encountering a rain cloud with a liquid water content (LWC) of 30 g/m^3 (corresponding to a rainfall rate of 39 in/hr) would experience an 18-percent increase in drag, a 29-percent reduction in maximum lift, and a 5° reduction in the angle of attack for maximum lift. These predictions constitute a substantial loss of performance.

At the time of the analysis by Haines and Luers, no experimental data existed for verification of the predictions; therefore in 1981 an experimental research program was established at Langley to obtain a data base for heavy rain effects. Small-scale wind tunnel tests were considered to provide the most controlled environment for evaluating the effect of rain on aerodynamics. Exploratory wind tunnel tests were conducted in 1982 in the Langley 14- by 22-Foot Subsonic Tunnel using an NACA 0012 airfoil section with a 14-in. chord which was fitted with a simple, full-span trailing-edge flap (ref. 8). The wind tunnel simulation technique produced the LWC concentrations found in convective thunderstorm rain clouds. This technique enabled the researchers to directly measure the simulated rain environment via the LWC parameter as detailed in references 8 and 9. The wind tunnel rain simulation system produced liquid water contents ranging from 13 to 22 g/m^3. A 15-percent reduction in the maximum lift of both the cruise and landing configurations of the airfoil model was measured independent of the liquid water content as shown in figure 1 at $q = 30$ psf and $N_{Re} = 1.7 \times 10^6$

In the mid-1980's, tests were conducted on an NACA 64-210 airfoil section (ref. 9) to determine the sensitivity of airfoil geometry to rain effects. An improved rain simulation system produced liquid water contents ranging from 16 to 46 g/m^3. Although both the cruise and landing configurations of the NACA 64-210 airfoil experienced significant losses in maximum lift capability and increases in drag with increasing LWC (fig. 2), the landing configuration was more sensitive to the rain environment than the cruise configuration. The landing configuration, which consisted of a leading-edge slat and a trailing-edge double-slotted flap, experienced a 22-percent reduction in maximum lift with an associated 8° decrease in the stall angle of attack at the highest LWC of 46 g/m^3 (approximately 59 in/hr) at $q = 30$ psf and $N_{Re} = 2.6 \times 10^6$, as shown in figure 2(b).

Both the NACA 64-210 and NACA 0012 airfoils exhibited significant reductions in maximum lift ca-

pability and increases in drag for a given lift condition in the simulated rain environment. The most significant difference between these two airfoil sections was the sensitivity of the NACA 64-210 airfoil section to increasing liquid water content. This difference indicated a rain effect sensitivity to camber. Note that the reduction in maximum lift (22 percent) and in the stall angle of attack (8°) for the NACA 64-210 landing configuration seriously reduced the airfoil design performance margin, which is defined as the performance delta between normal flight conditions and the aircraft stick-shaker condition, i.e., the angle of attack prior to stall.

Also in the mid-1980's, several types of airfoil sections were tested in simulated rain environments, both at Langley and at universities (refs. 10–12). The tests were divided among airfoils that had a significant amount of natural laminar flow (refs. 10 and 11) and airfoils that had transition fixed near the leading edge (refs. 11 and 12). The experimental results of the laminar flow airfoils indicated that the rain environment caused premature transition from a laminar to a turbulent boundary layer. Both the laminar and turbulent flow airfoils indicated significant losses in maximum lift and increases in drag. The rain environment induced an early separation in both the laminar and turbulent flow airfoils.

In summary, the small-scale wind tunnel tests to date have shown high-intensity rain to have an adverse effect on airfoil performance. The severity of this effect is dependent on the airfoil geometry and configuration and is most severe for airfoils with leading- and trailing-edge devices deployed. If the small-scale aerodynamic results are directly applicable to full-scale aircraft, then high-intensity rain would present a potential operational hazard. Specifically, the pilot of an aircraft encountering low-altitude wind shear during takeoff or landing operations would depend upon dry air performance margins for escape maneuvers. If the wind shear phenomenon is immersed in a severe rainstorm, the actual aircraft performance margin may be significantly reduced.

Because of the complexity of the water-air flow environment, the established laws for scaling a wind tunnel model to full scale may not be applicable in the rain environment. As noted in the work of Bilanin (ref. 13), difficulties arise when attempting to preserve all the scaling parameters critical to model testing in heavy rain. The characteristic Reynolds number of air, for example, is linearly dependent on the test velocity; therefore, as the model size is decreased, the test velocity must increase to preserve full-scale Reynolds number. On the other hand, the

Weber number of water (the ratio of the inertial forces to surface tension forces) varies as the square of the test velocity and, as a result, these two scaling parameters cannot be preserved simultaneously. Consequently, the acquisition of large-scale aerodynamic data in a simulated rain environment was identified as being necessary in assessing the sensitivity of the rain effect to model size.

The acquisition of large-scale aerodynamic data in a natural rain environment to validate the foregoing projections of degraded performance is a technical challenge. Although the ideal testing technique would be to fly an aircraft through a severe rainstorm and measure its performance, the extraction of accurate performance parameters while in a gusting, turbulent environment and the ability to repeat rain intensity conditions would be difficult, if not impossible, to achieve. As a result, NASA and the FAA developed a large-scale, ground-based test capability at the Langley Aircraft Landing Dynamics Facility (ALDF) in 1987. Figure 3 illustrates the research approach that was developed to exemplify an aircraft flying through a rainstorm. A wing is mounted on a test vehicle and is propelled along a track that travels through a highly concentrated rain field produced by a series of nozzles suspended above the track.

This paper focuses on the design methodology of the large-scale test capability. The ALDF rain simulation technique produced the rainfall intensities found in convective thunderstorm rain clouds. This technique enabled the researchers to directly measure the simulated rain environment via the rate at which rain falls. The ALDF test carriage modifications to transport a 10-ft-chord wing with a 13.1-ft span are described in detail along with the design, calibration, and operation of the 525-ft outdoor, overhead rain simulation system that produced rain fields of 2, 10, 30, and 40 in/hr. These rainfall rates are consistent with the airborne and ground-based rain intensity data measured in convective storms (refs. 4 and 5). The aerodynamic and rain simulation operating envelopes and the aerodynamic data acquisition and reduction processes are also discussed. Sample force data illustrating the environmental effects on data accuracy and repeatability for the dry ("rain-off") test condition are also presented.

Symbols and Abbreviations

A	collector box area
ALDF	Aircraft Landing Dynamics Facility
C_D	drag coefficient
C_L	lift coefficient
c	chord
c_d	section drag coefficient
c_l	section lift coefficient
d	exterior diameter of nozzle, in.
g	acceleration due to gravity ($1g \approx 32.174$ ft/sec^2)
L	sum of four vertical load cells
LWC	liquid water content, g/m^3
N_{Re}	Reynolds number
q	free-stream dynamic pressure
R	calculated rainfall rate
RSS	Rain Simulation System
S	area of wing
W_{water}	accumulated weight of water
α	angle of attack, deg
β	rain impact angle, deg
ρ_{water}	density of water

Subscript:

av	average

Test Facility

The Langley Aircraft Landing Dynamics Facility (ref. 14) was the test site chosen for developing the capability of acquiring large-scale aerodynamic data in a simulated rain environment. Although the ALDF, depicted in figures 4–7, was designed to test full-scale aircraft landing gear at operational velocities on a variety of simulated runway surfaces, the following features led to its selection:

1. The track length (3000 ft) was sufficient to incorporate a large-scale rain simulation system.

2. The test vehicle was large enough to support a large-scale wing section.

3. The facility had the capability of testing at speeds (up to 220 knots) comparable to commercial aircraft landing and takeoff conditions.

These operating characteristics facilitated the conversion of the ALDF to a large-scale, aerodynamic performance testing facility with minimal modifications to the test carriage and track test section. The test carriage was modified to incorporate a 10-ft-chord wing with a 13.1-ft span above the central open bay area of the carriage. The 1800-ft track

test section was modified to include an overhead rain simulation system along a 500-ft length of the track test section. These modifications allowed the facility to alternate between aerodynamic and landing-gear system testing with minimal conversion time. Both the landing-gear system and wing hardware remained mounted on the ALDF carriage, regardless of the experiment being conducted. The maximum allowable carriage test velocity, with the wing mounted, was 170 knots (287 ft/sec) because of wing construction constraints. Details on the ALDF test carriage, propulsion, and arrestment systems can be found in reference 14.

Test Article

The design, size, and location of the large-scale wing on the ALDF carriage were determined by considering the following factors: a representative, transport-type mean chord and airfoil section; similitude between the existing wind tunnel data base for heavy rain effects and the ALDF test; a mounting location within an area of undisturbed airflow; and carriage structural constraints.

Airfoil Geometry

The wing designed for testing at the ALDF was of rectangular planform and consisted of an NACA 64-210 airfoil section equipped with leading- and trailing-edge high-lift devices that could be configured to test cruise and landing conditions (fig. 8). The high-lift devices of the landing configuration consisted of a leading-edge slat deflected 57° and a trailing-edge double-slotted flap deflected 35.75°. The aerodynamic data acquired during this investigation were obtained on the landing configuration only for an angle-of-attack range from 7.5° to 19.5°. The ALDF wing chord was chosen to be 10 ft, which corresponded to a scaling factor of 4 when compared with the wind tunnel model chord of 2.5 ft (ref. 9). The ALDF wing airfoil section and wing configurations were identical to the small-scale wind tunnel model. The airfoil coordinates for the landing configuration are shown in tabular form in appendix A.

Wing Construction and Instrumentation

The ALDF wing structure was constructed based on a requirement to sustain high g-loads at launch (a maximum of 12.5g corresponding to a test velocity of 170 knots). The wing structure consisted of two spars, 13 aluminum ribs, and a 0.006-in-thick aluminum skin riveted in place as shown in figure 9. Figure 10 shows the assembled wing hardware in the landing configuration before installation onto the carriage structure. The forward spar and

the aft spar spanned the model at the 0.2729c and 0.7831c locations, respectively. (See fig. 11.) The ends of each spar were attached to a pair of strain-gauge load cells, one vertical and one horizontal, which were mounted on an I-beam structure as shown in figures 12 and 13. The vertical and horizontal load cells were positioned with respect to the wind axes to directly measure the lift and drag forces independent of the wing angle of attack. Because of the extreme g-loading at launch, the load cells were caged during catapult and released when the maximum carriage velocity was achieved.

Wing Location

The wing mounting location was determined by flow visualization techniques conducted on a 1/20th-scale model of the ALDF test carriage (fig. 14) in the Langley 12-Foot Low-Speed Tunnel. The test carriage, which is constructed of tubular members, is designed with an open bay area 40 ft long and 20 ft wide to accommodate tire testing hardware. The flow visualization studies, which were conducted at a dynamic pressure of 2 psf, investigated the influence of the carriage nose block and its accompanying tubular structure on the airflow at the proposed wing model location: at the top of the carriage rails above the central open bay area of the carriage as indicated in figure 15. The smoke visualization photographs in figures 16 and 17 indicate that the induced airflow disturbances of the carriage nose block would not significantly affect the airflow quality at the top of the carriage rails. These wind tunnel results were confirmed visually and photographically during a 160-knot test run on the ALDF with the rain simulation system turned on. In figure 18 the 40-in/hr rain field in front of the wing location is unaffected by the flow disturbances of the carriage nose block.

The wing mounting location that was chosen constrained the span of the wing to 13.1 ft, which corresponded to a geometric aspect ratio of 1.3. In order to minimize the amount of spanwise flow on the wing surface, 15-ft-diameter, circular endplates were mounted on either side of the wing model as shown in figures 19 and 20. The endplated ALDF wing had an effective aspect ratio of 4.15 based on Hoerner and Borst's relationship for geometric and effective aspect ratios of endplated wings (ref. 15). The endplates were constructed of 1-in-thick aluminum honeycomb panels and were supported by structural trusses attached to the carriage drop-rail supports. Figures 20 and 21 show the wing hardware mounted at a height of 22 ft above the track, near the top of the carriage drop rails and over the central open bay area of the carriage. The wing spars

pass through openings in the endplates, and the loads measured by the load cells are only those forces exerted by the wing section.

Rain Environment

The ALDF was selected as the test site because of the advantages of an outdoor rain simulation system compared with the indoor wind tunnel environment. The ALDF offered a more realistic depiction of an aircraft rain encounter, the capability of producing a greater range of raindrop sizes, and a minimization of the turbulent wake effects produced by the rain system hardware. The weather environment was considered to be the most critical problem associated with the design and operation of an outdoor rain simulation system. Freezing temperatures and high winds can severely affect the raindrop size distribution, rain field uniformity, and the accuracy of the aerodynamic measurement. The ALDF Rain Simulation System (RSS) was designed to minimize these concerns and meet the following technical requirements:

1. Produce rainfall intensities of 2 in/hr (with an LWC of 2 g/m^3), 10 in/hr (9 g/m^3), 30 in/hr (26 g/m^3), and 40 in/hr (35 g/m^3).

2. Maintain uniformity of the rain field along and across the track test section within ±10 percent.

3. Produce a raindrop size distribution of 0.5 to 4.0 mm.

4. Achieve raindrop terminal velocities within ±10 percent of the nominal values.

As observed in the wind tunnel rain simulation tests, the size of the raindrops produced is a function of the difference between the drop and airstream velocities and the operating pressure at the nozzle exit. The task of achieving a desired drop size and distribution becomes more difficult with the additional requirement of simultaneously varying the drop size and the intensity levels of the rainfall concentration. Low operating pressures are desirable to prevent the formation of too many small drops (less than 1 mm) as was the case in the wind tunnel simulation technique (ref. 9). Consequently, the drop size distribution and the rainfall intensity requirements were chosen to achieve the following criteria: represent drop sizes found in rainstorms that could be produced by commercially available nozzles, match rainfall concentrations produced in the wind tunnel (26 and 35 g/m^3), and simulate lower rainfall concentrations (2 and 9 g/m^3) than could be achieved by the wind tunnel technique.

Design Concepts

Two types of rain distribution systems were considered: a ground-based system and an overhead system suspended above the track test section. Several factors determined the selection of an overhead system instead of the ground-based system. Particular attention was focused on the capability of each system to ensure uniform area coverage at the various intensity levels of rainfall concentration in a windy environment. The overhead system was less sensitive to the wind environment than the ground-based system. The ground-based system required the raindrops to follow a parabolic trajectory versus the vertical path produced by the overhead system. Drifts in the vertical path, which could disrupt the lateral (across the track) uniformity of the rain field, could be compensated for by extending the width of the simulated rain field. This feature could be more easily accomplished with an overhead system. Another consideration leading to the ultimate selection of the overhead system was the availability of commercial irrigation hardware that could be adapted to the required specifications rather than designing an entirely new system for one-time usage. An industry survey of available hardware was conducted which indicated that an agricultural, irrigation-type overhead system would be the most economical and feasible design.

Selected Concept

An illustration of the ALDF RSS concept is shown in figure 22. The overhead-based distribution system would consist of several irrigation pipes positioned lengthwise along the ALDF track test section and supported at both ends by a structural support tower. The width of the ALDF RSS was sized to ensure full-model immersion during testing. One leg of the structural support tower allowed the flow of water to travel from the water-air supply system up to the irrigation pipes. Feeding off each irrigation pipe would be a series of drop-pipe assemblies oriented perpendicular to the track. The longitudinal (along-the-track) spacing of the pipes was dependent upon the desired rainfall rate. The rain spray nozzles were located at both ends of the pipe assemblies. A low-pressure water distribution system was identified as being beneficial in keeping the complexity and cost of the system reasonable.

ALDF RSS Design Prototype

A prototype 105-ft section of the proposed ALDF RSS design was constructed and tested at the NASA Wallops Flight Facility to provide rain field performance data required to verify that the design of the

system meets the established requirements (ref. 16). The prototype system consisted of three 105-ft-long commercial irrigation pipes, each supported by a triangular-shaped structure on either end as shown in figure 23. The prototype system was supplied by a nearby fire hydrant that allowed for continuous low-pressure operations to facilitate data collection and system observation. The candidate nozzles were suspended 14 ft above the ground to allow sufficient time for the raindrops to achieve terminal velocity within ±10 percent of the nominal values. The prototype system produced a uniform simulated rain field 30 ft in width and 100 ft in length.

The development testing included single-nozzle tests to determine the radial distribution pattern and rain intensities of the candidate nozzles. The results from the single-nozzle tests were used in a computer program developed to summarize the rain intensity from each of the contributing nozzles to simulate the performance of the rain system. This program was used for a parametric study of candidate nozzles (defined by rain intensity and radial distribution pattern) and nozzle spacing (both along and across the rain system) to determine a combination that would produce the desired rain rate within an intensity distribution pattern of ±10 percent. Full-cone nozzles were found to meet the requirements on the spray distribution pattern, rain intensity, drop sizes, and uniformity. Based on the manufacturer's data, these nozzles produced drop sizes within the desired range (from 0.5 to 4.0 mm with a volumetric mean drop diameter, the diameter at which half the volume of the spray is in drops larger or smaller than 2 mm) at nozzle pressures between 6 and 12 psig.

The development testing identified the following modifications to the final design of the ALDF RSS:

1. The 40-in/hr nozzles were installed with a specific orientation with respect to the internal construction of the nozzle in order to produce a rainfall rate distribution within the ±10-percent limit. These nozzles were installed with every other row having the orientation centerline perpendicular to the orientation of the previous row as shown in figure 24.

2. In order to maintain 10 psig at the nozzle regulator, two water-air supply stations were needed to fill a 105-ft section. Each water-air supply station filled one-half of two 105-ft sections for a total of six water-air supply stations for the entire system.

The measured rain rate distributions resulting from the development tests on the prototype system

for the four rainfall rates are presented in figure 25. Table I summarizes the spacing between the spray nozzles along and across the system for the corresponding nozzle type and water concentration level.

Required Length of the ALDF RSS

Once an overhead-based distribution system was chosen as the rain simulation technique, the system length necessary to accurately simulate the aerodynamic losses in the heavy rain environment had to be determined. A wind tunnel investigation (fig. 26) was conducted in the Langley 14- by 22-Foot Subsonic Tunnel for the purpose of determining the time required for the aerodynamic forces of a simple wing model to transition from dry steady-state conditions to wet steady-state conditions (ref. 12). The model used in this investigation consisted of a rectangular wing mounted to a fuselage. The wing had an NACA 23015 airfoil section, a 1.29-ft chord, and a 7.88-ft span. A piezoelectric device was installed on the nose of the fuselage (fig. 27) to signal the onset of the rain spray immersing the model. The determination of the transition time from dry steady-state to wet steady-state conditions provided the guidelines for determining the minimum rain field length necessary for the effect of rain to be measurable.

The data used to establish the transition time were derived from the oscillographic traces of normal force and the piezoelectric device near the stall angle of attack. The vertical lines of the oscillographic trace shown in figure 28 denote 0.1-sec increments. Because the piezoelectric device was attached to the most forward model location, the precise time that water impacts the model is indicated by the increased activity in its trace. The example shown denotes approximately a 0.2-sec transition time for the normal force to leave its dry steady-state value and achieve its wet steady-state value, i.e., a fully developed water film pattern on the wing surfaces for a dynamic pressure of 50 psf (205 ft/sec), an angle of attack of 16°, and a liquid water content of 22 g/m³. Repeat runs at the same test conditions revealed some variations in the transition time with the average value for the above test condition being on the order of 0.3 sec.

By knowing the wind tunnel test velocity, the model chord, and the transition time, the number of chords traversed by the wind tunnel model during its establishment of the new, wet steady-state condition was calculated. These calculations yielded 48 chords traversed during the transition. To determine the length of the ALDF RSS, the nondimensional number of chords traversed for the wind tunnel model was equated to the chords traversed by the ALDF

model. Given the ALDF wing model chord of 10 ft, a minimum distance of 480 ft was calculated as being necessary to achieve a wet steady-state performance level at a liquid water content of 22 g/m^3.

The wind tunnel results provided only transition time guidelines for the higher requirements on water concentration level. The work of Bilanin, Quackenbush, and Feo (ref. 17) addressed the transition times for the lower requirements on water concentration level. Bilanin analytically estimated the time required to form a fully developed water film upon a flat plate at various water concentration levels. The data in figure 29 indicate that the time needed to develop 90 percent of the water film thickness on a horizontal flat plate decreased hyperbolically with increasing rainfall rate. Bilanin calculated that for a 170-knot wind, the corresponding times for rainfall rates of 2 in/hr and 50 in/hr were 6.7 sec and 0.77 sec, respectively. Bilanin's results translated to rain system lengths of 1921 ft and 221 ft, respectively, for the aforementioned test conditions.

The wind tunnel results and analytical calculations bracketed the rain system length for the rain field intensities required to be between 221 ft (at a rate of 50 in/hr) and 1921 ft (at a rate of 2 in/hr). The track test section constraints and financial considerations narrowed the length of the rain simulation system to 500 ft. The research staff acknowledged that at the lower rainfall rates of 2 and 10 in/hr, the effect of rain might not reach a steady-state value. The consensus was that the adverse effect of rain on airfoil aerodynamics occurs at high-intensity rainfall rates and that the 500-ft length is sufficient to measure the steady-state aerodynamic losses at 30 and 40 in/hr. A review of the agricultural community on irrigation hardware resulted in constructing the ALDF RSS in 105-ft sections for a total of five sections (525 ft).

Required Width of the ALDF RSS

Wind effects are by far the most predominant environmental consideration for outdoor testing in heavy rain. Both steady and gusting winds have to be taken into account when determining rain field uniformity and data reduction and analysis. The wind velocity at the ALDF was measured by two commercial wind anemometers (fig. 30) located 250 ft down track from the beginning of the RSS. Anemometers were located on either side of the RSS at the same height as the wing. A digital display provided instantaneous readouts of wind speed and direction. During the RSS prototype development, the rain rate did not change significantly because

of wind, but the rain field was shifted horizontally across the system because of crosswind conditions (figs. 31 and 32). In order to assure that the simulated rain field was not transported out of the test region, an operational limit on the maximum allowable crosswind was set at 5 ft/sec. Based on a review of the literature on the angle of inclination for raindrop sizes as a function of wind speed (ref. 18), the displacement due to the crosswind was calculated for the 14-ft distance from the nozzle to the wing surface. The displacement of the smaller drops, which are most susceptible to crosswind, was 6 to 7 ft. Therefore, the design width of the uniform rain was the width of the model, endplates, and truss support structure plus an additional 7.5 ft on each side of the model for a total width of 30 ft. Shifts in the rain field due to a 5-ft/sec crosswind did not affect the rainfall rate over the wing location.

Because of the 5-ft/sec crosswind limit, knowing the crosswind component relative to the ALDF track was necessary at all times. This was facilitated by a computer program that sampled the wind anemometers as frequently as every second to determine a launch/no-launch judgment. Carriage structural constraints limited head and tail winds to a 25-ft/sec limit.

The ALDF RSS

The ALDF RSS simulates a thunderstorm-type rain which is defined as being a high-intensity, short-duration rainfall. The ALDF RSS utilized nozzles suspended 40 ft above the ALDF track to produce uniform simulated rainfall rates of 2, 10, 30, and 40 in/hr over an area 30 ft wide (centered across the track) by 525 ft long (along the track). Different rainfall rates were obtained by configuration changes of nozzle size and/or nozzle spacing. Figures 33 and 34 are photographs showing the intensity of the rain field produced by the ALDF RSS at 40 in/hr. The ALDF RSS was designed to allow passage of the carriage-wing section assemblage through the simulated rain with the wing section located 14 ft below the nozzles. This spacing allowed the drops to achieve terminal velocity for more accurate simulation of naturally occurring, free-falling rain as shown in table II (a theoretical velocity chart).

The ALDF RSS consisted of five 105-ft-long sections as shown in figure 35. Each section consisted of three parallel 10-in-diameter irrigation pipes spaced 15 ft apart and aligned lengthwise along the ALDF track. The irrigation pipes were supported at each end by 14-in-diameter pipes called "support towers." One leg of each support tower acted as a supply leg to transport water from the water-air supply stations

to the irrigation pipes. Drop-pipe assemblies were located every 2 ft along the irrigation pipe of the ALDF RSS. This spacing was determined to be adequate for producing the simulated rain environments specified. Each drop-pipe assembly (see fig. 36) consisted of a check valve, a 10-psi pressure regulator, and two nozzle locations (one on either end of the pipe). A pair of full-cone nozzles or plugs, depending on the desired rain rate configuration, was attached to the drop-pipe assembly to provide a simulated rain field. The check valve prevented drainage of the system, and the pressure regulator maintained operating pressure.

Water for the ALDF RSS was supplied by six water-air supply stations. Each station consisted of a 1000-gal water storage tank that was regulated to 80 psig by means of air from a 300-psig air accumulator (fig. 37). Six remotely operated 10-in-diameter butterfly valves (with one located between each water tank and the supply leg) acted as the on/off control valve for the ALDF RSS. Two water-air supply stations fed each support tower leg in order to fill the system.

ALDF RSS Calibration

A simple calibration technique to measure rainfall rate, which was developed during the prototype testing of the ALDF RSS design, involved the use of a series of large collector cans (4.16 in. in diameter) spaced in 1-ft increments along and across the track. The cans were fitted with drain valves and were suspended at the equivalent wing model height of 14 ft (figs. 33 and 38). After each cycle (i.e., on/off) of the RSS, the accumulated volume of each can was measured via graduated cylinders and was related to a rainfall rate based on the cycle time of the RSS. This method provided both rainfall rate and uniformity data. Precautionary measures were implemented to minimize technique measurement errors. The collector cans were prewetted with the drain valves open just prior to use to eliminate dry surfaces that could cause water adhesion and thereby cause lower than actual readings. Calibration data were collected over several minutes to minimize the effect of water accumulated both before achieving a uniform rain field and after turning the water off. Sample uniformity curves using the aforementioned technique are shown in figure 39 for the ALDF RSS at the 40-in/hr rainfall rate.

To provide an alternate method to characterize the rain environment, a ground-based weight-measuring system was developed by the NASA Wallops Flight Facility (ref. 19) during the prototype testing of the ALDF RSS design. The system designed was a weight-measuring gauge in which the collected rain was funneled into a 1-ft^2 container that was mounted on a platform-scale load cell as shown in figure 40. All the calibration data were acquired during low-wind conditions corresponding to the maximum allowable crosswind component of 5 ft/sec.

The rain gauge system was powered by a 10-V direct-current power supply. Data from the load cell were fed by a cable to a digital voltmeter through an amplifier. The data were transferred from the voltmeter to a computer at a sample rate determined by the system user. The rainfall rate was then calculated from these data.

The operation of the weight-measuring rain gauge was based on the equation

$$R = \frac{1}{Ag\rho_{\text{water}}} \frac{\Delta W_{\text{water}}}{\Delta t}$$

where

R	calculated rainfall rate
W_{water}	accumulated weight of water
A	collector box area
g	acceleration due to gravity $(1g \approx 32.174 \text{ ft/sec}^2)$
ρ_{water}	density of water
t	time

The weight-measuring system was designed to operate in two modes, a rain search mode and a data acquisition mode. In the rain search mode, the computer sampled the load cell to determine if the weight had increased, thus implying that rain was present. Once the computer had determined that a delta weight threshold had been exceeded, the software would switch to a data acquisition mode and record data for 20 minutes before returning to the rain search mode. This method of operation allowed for the time interval of interest, i.e., the period when rain had fallen, to be isolated for analysis. Because the ALDF RSS generated a maximum rainfall rate of 40 in/hr (1016 mm/hr) for a duration of approximately 20 sec, the weight-measuring rain gauge system was designed to take a weight measurement as often as once per second and could be programmed for a variable sample rate. For example, a 15-sec segment during a fully developed, simulated rain field sequence could be analyzed separately, and thereby eliminate water on/off errors.

When positioning either the weight-measuring rain gauge or the can collectors, care was taken so as not to locate them directly beneath a nozzle. This

precaution avoided false readings resulting from water dripping from the system before and after each cycle. A comparison of the measurements obtained from the rain gauge and collector cans shows good agreement as shown in figure 39.

Rain Characterization

The measurement of the raindrop distribution was also an important aspect of the ALDF RSS calibration. An attempt was made to use a conventional, high-speed, flash photographic technique to provide these data; however, incomplete illumination of individual drops, in addition to inadequate depth of field, led to the development of a shadowgraph technique (fig. 41). The shadowgraph system consisted of a high-pressure, pulsed, point light source of 100-W xenon, a 6-in-diameter source collimating lens, a 6-in-source focusing lens, and a 70-mm camera. The 6-in-diameter lenses were used to produce parallel light within the controlled sample region. Having parallel light, the shadows cast by the drops provided accurate drop size measurements. The light source and the camera were synchronized and remotely controlled to take pictures only during the time corresponding to a fully developed rain field.

Figure 42 depicts the rain shield used to protect the instrumentation. An adjustable slot at the top of the shield admits the rain to be photographed. A typical photograph taken at 40 in/hr (1016 mm/hr) is shown in figure 43. The values of drop size and drop size distribution are determined with the aid of computer digitization and enhancement techniques. Figure 40 shows drops ranging from approximately 0.3 to 4.5 mm. However, analysis reveals a substantially higher number of drops compared with that predicted by the Marshall-Palmer distribution (ref. 20). The Marshall-Palmer distribution of reference 20 is based on raindrop-size measurements found in light, continuous rainstorms and may not accurately depict raindrop sizes found in convective thunderstorm rain environments (refs. 2 and 3). Also, uncertainties are involved with the digitization resolution, drops splashing on top of the rain shield, and/or wind-induced drops impacting the inner sidewalls of the shield.

Data Acquisition and Reduction Process

The ALDF data acquisition system consisted of a 28-channel, 12-bit telemetry system with a frame rate of 1066 frames per second. The data were transmitted from the test carriage to a telemetry receiver that was linked to a personal computer. Active low-pass filters with a cutoff frequency of 100 Hz were utilized at the signal conditioning stage

before the data were telemetered to the receiving station. The received binary data were then written to floppy disks for subsequent analysis.

The transducer outputs necessary for the required calculations of model lift and drag were as follows: (1) vertical and longitudinal load-cell force measurements; (2) vertical and longitudinal acceleration measurements; (3) roll-, pitch-, and yaw-rate measurements; and (4) free-stream dynamic pressure. Although carriage velocity was measured directly by a proximity probe, a determination was made early in the test program that a more accurate measurement of the airspeed experienced by the wing section was required. Therefore, an aircraft Pitot-static tube was mounted on the forward extremity of the carriage as shown in figure 44. The direct measurement of free-stream dynamic pressure took into account the wind environment present during a test run. The wind direction and magnitude, temperature, and barometric pressure were also recorded at the time of launch. The list of measurements is shown in table III.

The quantities of lift and drag were calculated by the equations detailed in appendix B. Preliminary checkout runs showed that the vibratory forces exerted on the wing model, as measured by the accelerometers and rate gyros, were of high frequency and that their effect on the aerodynamic lift data was negligible. (See appendix B.) The lift data were then digitally filtered with a low-pass filter (a cutoff frequency of 1/2 Hz) to remove the structural vibrations. This simplified the calculation of lift to a summation of the four vertical load-cell readings to determine the total lift force. However, the net deceleration loads were large and had to be accounted for in the drag equation. The resultant net drag force was the difference between the inertial and longitudinal aerodynamic forces. This small difference between two large numbers yielded unreliable drag measurements; therefore, drag data are not presented in this paper.

The section lift coefficient was calculated from the relationship

$$c_l = \frac{L}{qS}$$

where L denotes the sum of the four vertical load cells, S denotes the area of the wing, and q denotes the free-stream dynamic pressure. The free-stream dynamic pressure was measured directly by the Pitot-static system by taking into account variations in local density ρ (less than a 4-percent increase at the 40-in/hr rainfall condition).

Environmental Effects on Aerodynamic Data

As mentioned earlier, wind effects are by far the predominant environmental consideration for outdoor investigations in heavy rain. Hence, another consideration of wind effects involves the aerodynamic performance of the wing. The "water-off" (or dry) angle-of-attack case of 9.5° is shown in figures 45–50 to illustrate the effect of variable crosswinds on the data. The aerodynamic data were calculated between approximately 3 and 8 sec after launch.

A plot of airspeed calculated from the measured dynamic pressure is shown in figure 45 for a calm wind condition. The initial peak of the curve results from the acceleration pulse. This is followed by the gradual slope caused by the carriage deceleration, then the sudden decrease during arrestment. Figures 46 and 47 show the total lift and lift coefficient data (time-averaged $c_l = 2.36$), respectively, for a dry wing in a typical calm wind condition (i.e., no crosswind present), all as a function of time. The effects on airspeed produced by a crosswind having an average velocity of 5 ft/sec at 280° are depicted in figures 48–50. The wind-velocity perturbations are seen by oscillations of airspeed in figure 48. The corresponding total lift (fig. 49), which was measured directly by means of the load cells, similarly shows the dynamic response to these gusts. This results in the nonlinearity of the c_l plot shown in figure 50. In most cases, the wind caused the resulting mean value of c_l to lie outside the desirable 1.5-percent accuracy margin of the calm wind condition of c_l (2.32 to 2.39). However, similar oscillatory effects were also observed for a small head wind of 5.4 ft/sec at 28° as depicted in figure 50, but the mean c_l of 2.38 is within limits. This indicates that each c_l plot must be analyzed individually for wind effects. Hence, the acquisition of repeatable data requires low wind velocities and minimal changes in wind direction during a run, as depicted in the case of the 3-ft/sec wind at a constant 211°, where the mean c_l value of 2.33 is within acceptable limits.

Another environmental consideration involves changes in temperature. The pressure transducers of the Pitot-static tube are temperature sensitive. Hence, temperature fluctuations may cause electronic zero shifts in the instrumentation. This effect was accounted for by taking new electronic zeros just prior to each launch of the carriage. The collection of dew on the wing surface has the effect of prewetting the wing. This may change the

dry-to-wet wing transitional aerodynamics by altering the time required for the water film pattern to develop as mentioned in reference 11. As a precaution, the ALDF carriage-wing assemblage was stored in a hangar overnight and was not tested during rain showers or thunderstorms.

Concluding Remarks

A research technique was developed at the Langley Aircraft Landing Dynamics Facility (ALDF) for providing quality aerodynamic data and realistic rainfall intensities as seen during a simulated thunderstorm-type rain encounter. The test carriage of the facility was modified to transport a 10-ft-chord NACA 64-210 wing section, representative of modern-day transports, along a 3000-ft track at full-scale aircraft approach speeds. An overhead rain simulation system was constructed along a 525-ft section of the track test section to produce simulated rain fields of 2, 10, 30, and 40 in/hr. The NACA 64-210 wing was tested with high-lift devices deployed to simulate landing conditions.

To assure similitude between the existing wind tunnel data base and the ALDF data base, the following parameters were matched: airfoil section, model configuration, angle of attack, and testing environment. The wing angle of attack, which could be fixed at one angle setting per test run, was varied from 7.5° to 19.5° in 2° increments. The ALDF had the capability of operating the modified carriage as slow as 100 knots (168 ft/sec) and as fast as 170 knots (287 ft/sec), which encompassed the wind tunnel operating range of 168 to 205 ft/sec and aircraft approach and takeoff velocities. The ALDF Rain Simulation System (RSS) liquid water contents of 26 and 35 g/m^3 (corresponding to 30 and 40 in/hr, respectively) matched simulated wind tunnel rain conditions. Aerodynamic data were acquired on the landing configuration at five test conditions (dry air, and 2, 10, 30, and 40 in/hr) and eight angles of attack per test condition.

The effect of high winds on the intensity and uniformity of the rain field was incorporated into the design of the ALDF RSS. Wind limits were placed on the operation of the RSS and on the acquisition of aerodynamic data to ensure quality aerodynamic measurements. The design of the large-scale wing section ensured the consistency between this data base and the small-scale wind tunnel data base.

The development of this aerodynamic rain testing facility will aid in the assessment of the rain hazard at large-scale conditions and will provide data for the development and validation of scaling relationships for testing models in heavy rain.

NASA Langley Research Center
Hampton, VA 23681-0001
March 5, 1993

Appendix A

NACA 64-210 Airfoil Coordinates

The geometric coordinates of the landing configuration of the 10-ft-chord NASA 64-210 wing are presented in tabular form in this appendix. The coordinates are given in percent chord, based on the wing chord of 10 ft, for each high-lift device and main wing section.

Table A1. Leading-Edge Slat Coordinates

Upper surface		Lower surface	
$\frac{x}{c} \times 100$	$\frac{z}{c} \times 100$	$\frac{x}{c} \times 100$	$\frac{z}{c} \times 100$
0	0	0	0
.0097	.1395	.0123	−.1654
.0402	.2759	.0459	−.3279
.0941	.4049	.0966	−.4859
.1695	.5226	.1609	−.6389
.2614	.6280	.2366	−.7866
.3659	.7210	.3217	−.9292
.4799	.8021	.4143	−1.0669
.6012	.8717	.5123	−1.2009
.7284	.9302	.6148	−1.3315
.8598	.9782	.7209	−1.4592
.9941	1.0174	.8301	−1.5842
1.1304	1.0489	.9421	−1.7067
1.2681	1.0744	1.0567	−1.8268
1.4065	1.0946	1.1734	−1.9449
1.5456	1.1104	1.2921	−2.0610
1.6851	1.1222	1.4125	−2.1752
1.8247	1.1307	1.5345	−2.2879
1.9646	1.1361	1.6577	−2.3991
2.1045	1.1388	1.7820	−2.5092
2.2445	1.1389	(a)	(a)
2.3844	1.1366	1.8369	−2.4013
2.5243	1.1320	1.7742	−2.2533
2.6641	1.1252	1.7322	−2.0997
2.8038	1.1163	1.7125	−1.9418
2.9433	1.1055	1.7162	−1.7826
3.0827	1.0932	1.7437	−1.6259
3.2220	1.0795	1.7939	−1.4748
3.3612	1.0646	1.8645	−1.3321
3.5002	1.0487	1.9518	−1.1989
3.6391	1.0318	2.0535	−1.0764
3.7780	1.0142	2.1682	−.9659
3.9167	.9959	2.2950	−.8696
4.0554	.9770	2.4324	−.7891
4.1940	.9575	2.5770	−.7222

Upper surface		Lower surface	
$\frac{x}{c} \times 100$	$\frac{z}{c} \times 100$	$\frac{x}{c} \times 100$	$\frac{z}{c} \times 100$
4.3325	0.9374	2.7262	−0.6665
4.4709	.9167	2.8793	−.6224
4.6093	.8955	3.0340	−.5844
4.7475	.8736	3.1898	−.5513
4.8856	.8511	3.3465	−.5228
5.0237	.8281	3.5039	−.4982
5.1616	.8045	3.6617	−.4765
5.2995	.7804	3.8198	−.4573
5.4373	.7558	3.9782	−.4399
5.5749	.7306	4.1367	−.4244
5.7125	.7049	4.2954	−.4106
5.8500	.6788	4.4542	−.3984
5.9874	.6522	4.6132	−.3878
6.1247	.6251	4.7722	−.3787
6.2620	.5976	4.9313	−.3709
6.3991	.5696	5.0904	−.3643
6.5361	.5412	5.2497	−.3589
6.6731	.5124	5.4089	−.3547
6.8099	.4831	5.5682	−.3515
6.9467	.4534	5.7276	−.3494
7.0834	.4234	5.8869	−.3482
7.2200	.3929	6.0462	−.3479
7.3565	.3621	6.2055	−.3483
7.4930	.3309	6.3648	−.3496
7.6293	.2994	6.5241	−.3516
7.7656	.2674	6.6834	−.3545
7.9018	.2352	6.8427	−.3581
8.0379	.2026	7.0020	−.3627
8.1739	.1697	7.1612	−.3681
8.3098	.1364	7.3204	−.3745
8.4457	.1029	7.4796	−.3819
8.5815	.0690	7.6387	−.3902
8.7173	.0348	7.7977	−.3998
8.8529	.0004	7.9566	−.4109
8.9885	−.0343	8.1154	−.4236
9.1240	−.0693	8.2741	−.4380
9.2594	−.1046	8.4327	−.4539
9.3948	−.1401	8.5910	−.4712
9.5301	−.1758	8.7493	−.4899
9.6654	−.2118	8.9073	−.5097
9.8006	−.2481	9.0653	−.5308
9.9357	−.2845	9.2231	−.5529
10.0707	−.3212	9.3807	−.5760
10.2057	−.3581	9.5382	−.6000
10.3407	−.3952	9.6956	−.6249

Table A1. Concluded

Upper surface		Lower surface	
$\frac{x}{c} \times 100$	$\frac{z}{c} \times 100$	$\frac{x}{c} \times 100$	$\frac{z}{c} \times 100$
10.4756	−0.4326	9.8528	−0.6504
10.6104	−.4701	10.0100	−.6764
10.7452	−.5079	10.1671	−.7031
10.8799	−.5458	10.3241	−.7302
11.0145	−.5840	10.4810	−.7576
11.1491	−.6224	10.6379	−.7853
11.2837	−.6609	10.7947	−.8137
11.4182	−.6996	10.9513	−.8430
11.5526	−.7385	11.1077	−.8734
11.6869	−.7776	11.2639	−.9048
11.8213	−.8169	11.4200	−.9370
11.9556	−.8564	11.5758	−.9698
12.0898	−.8961	11.7316	−1.0034
12.2240	−.9359	11.8872	−1.0376
12.3581	−.9760	12.0427	−1.0722
12.4921	−1.0163	12.1981	−1.1073
12.6261	−1.0567	12.3535	−1.1427
12.7600	−1.0973	12.5088	−1.1782
12.8939	−1.1379	12.6640	−1.2140
13.0294	−1.1791	12.8193	−1.2499
		12.9745	−1.2858

[a]Break in lower surface contour:

Break
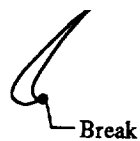
Table A2. Main Wing Section Coordinates

Upper surface		Lower surface	
$\frac{x}{c} \times 100$	$\frac{z}{c} \times 100$	$\frac{x}{c} \times 100$	$\frac{z}{c} \times 100$
0	0	0	0
.3704	.9455	.4139	−.8681
1.1669	1.6095	1.3173	−1.2357
2.0441	2.1662	2.2819	−1.4412
2.9528	2.6700	3.2505	−1.6265
3.8808	3.1375	4.2224	−1.7943
4.8251	3.5710	5.1967	−1.9473
5.7912	3.9532	6.1728	−2.0884
6.7756	4.2859	7.1504	−2.2191
7.7686	4.5920	8.1290	−2.3417
8.7707	4.8666	9.1085	−2.4572
9.7780	5.1219	10.0887	−2.5661
10.7846	5.3798	11.0696	−2.6691
11.8011	5.5941	12.0510	−2.7666
12.8287	5.7484	13.0330	−2.8588
13.8567	5.9004	14.0154	−2.9461
14.8854	6.0474	14.9981	−3.0289
15.9153	6.1850	15.9812	−3.1076
16.9461	6.3168	16.9646	−3.1824
17.9775	6.4428	17.9482	−3.2534
19.0099	6.5610	18.9321	−3.3205
20.0427	6.6756	19.9162	−3.3842
21.0760	6.7856	20.9006	−3.4448
22.1100	6.8887	21.8851	−3.5016
23.1443	6.9882	22.8699	−3.5554
24.1792	7.0821	23.8547	−3.6072
25.2145	7.1711	24.8397	−3.6561
26.2502	7.2553	25.8248	−3.7013
27.2863	7.3348	26.8101	−3.7432
28.3227	7.4096	27.7955	−3.7824
29.3595	7.4795	28.7811	−3.8187
30.3965	7.5448	29.7667	−3.8522
31.4339	7.6056	30.7524	−3.8827
32.4715	7.6619	31.7382	−3.9105
33.5093	7.7138	32.7241	−3.9356
34.5474	7.7611	33.7100	−3.9577
35.5856	7.8044	34.6961	−3.9764
36.6240	7.8426	35.6821	−3.9927
37.6626	7.8764	36.6682	−4.0068
38.7013	7.9065	37.6544	−4.0175
39.7401	7.9320	38.6405	−4.0248
40.7790	7.9520	39.6267	−4.0298
41.8180	7.9671	40.6129	−4.0322
42.8571	7.9773	41.5991	−4.0306
43.8962	7.9823	42.5853	−4.0248
44.9353	7.9820	43.5714	−4.0155

Upper surface		Lower surface	
$\frac{x}{c} \times 100$	$\frac{z}{c} \times 100$	$\frac{x}{c} \times 100$	$\frac{z}{c} \times 100$
45.9744	7.9760	44.5575	−4.0026
47.0135	7.9644	45.5436	−3.9857
48.0525	7.9468	46.5296	−3.9648
49.0913	7.9231	47.5154	−3.9398
50.1300	7.8937	48.5012	−3.9104
51.1686	7.8586	49.4868	−3.8768
52.2069	7.8176	50.4723	−3.8389
53.2450	7.7723	51.4576	−3.7971
54.2830	7.7234	52.4427	−3.7518
55.3207	7.6701	53.4277	−3.7033
56.3583	7.6128	54.4126	−3.6514
57.3956	7.5523	55.3972	−3.5965
58.4328	7.4880	56.3818	−3.5400
59.4697	7.4201	57.3663	−3.4815
60.5064	7.3489	58.3506	−3.4209
61.5428	7.2743	59.3348	−3.3580
62.5790	7.1964	60.3188	−3.2927
63.6149	7.1152	61.3027	−3.2250
64.6506	7.0308	62.2864	−3.1553
65.6861	6.9434	63.2700	−3.0839
66.7213	6.8533	64.2538	−3.0109
67.7563	6.7604	65.2375	−2.9360
68.7909	6.6644	66.2210	−2.8595
69.8253	6.5649	67.2043	−2.7815
70.8594	6.4632	68.1876	−2.7020
71.8934	6.3601	69.1708	−2.6211
72.9272	6.2545	70.1538	−2.5389
73.9606	6.1461	71.1368	−2.4556
74.9938	6.0349	72.1196	−2.3710
76.0267	5.9218	73.1024	−2.2856
77.0595	5.8070	74.0851	−2.1990
78.0920	5.6898	75.0677	−2.1114
79.1242	5.5706	76.0502	−2.0230
80.1563	5.4497	77.0326	−1.9338
81.1882	5.3272	78.0150	−1.8439
82.2199	5.2034	78.9973	−1.7533
83.2515	5.0785	79.9796	−1.6622
84.2830	4.9525	80.9618	−1.5707
85.3143	4.8257	81.9440	−1.4789
86.3456	4.6984	82.9262	−1.3868
87.3769	4.5707	83.9083	−1.2947
88.4081	4.4427	84.8905	−1.2024
89.4393	4.3146	85.8727	−1.1101
90.4705	4.1868	86.8548	−1.0180

Table A2. Concluded

Upper surface		Lower surface	
$\frac{x}{c} \times 100$	$\frac{z}{c} \times 100$	$\frac{x}{c} \times 100$	$\frac{z}{c} \times 100$
91.5018	4.0591	87.8370	−0.9261
92.5330	3.9316	88.8192	−.8344
93.5643	3.8043	89.8014	−.7429
94.5956	3.6770	90.7837	−.6519
95.6269	3.5498	91.7661	−.5615
96.6582	3.4226	92.7485	−.4719
97.6895	3.2954	93.7310	−.3834
98.7208	3.1682	94.7136	−.2965
99.7522	3.0410	95.6964	−.2112
100.8750	2.9025	96.8950	−.1099
		[a]96.8950	[a]−.1099
		[a]96.9920	[a].1507
		[a]97.1048	[a].4044
		[a]97.2343	[a].6501
		[a]97.3807	[a].8861
		[a]97.5422	[a]1.1121
		[a]97.7174	[a]1.3275
		[a]97.9053	[a]1.5321
		[a]98.1053	[a]1.7248
		[a]98.3170	[a]1.9045
		[a]98.5396	[a]2.0706
		[a]98.7721	[a]2.2225
		[a]99.0137	[a]2.3595
		[a]99.2634	[a]2.4811
		[a]99.5202	[a]2.5867
		[a]99.7832	[a]2.6762
		[a]100.0510	[a]2.7496
		[a]100.3230	[a]2.8060
		[a]100.5980	[a]2.8434
		[a]100.8750	[a]2.8657

[a]Lower surface cove coordinates:

Lower surface cove

17
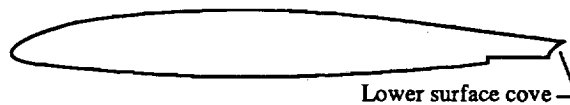
Table A3. Trailing-Edge Vane Coordinates

Upper surface		Lower surface	
$\frac{x}{c} \times 100$	$\frac{z}{c} \times 100$	$\frac{x}{c} \times 100$	$\frac{z}{c} \times 100$
0	0	0	0
.0042	.1092	.0092	−.1057
.0170	.2177	.0268	−.2139
.0384	.3248	.0535	−.3201
.0687	.4298	.0893	−.4236
.1074	.5320	.1341	−.5235
.1544	.6306	.1879	−.6189
.2093	.7251	.2507	−.7086
.2714	.8151	.3225	−.7914
.3397	.9003	.4030	−.8656
.4137	.9807	.4915	−.9301
.4932	1.0556	.5870	−.9836
.5779	1.1248	.6884	−1.0250
.6671	1.1878	.7939	−1.0543
.7605	1.2446	.9020	−1.0721
.8573	1.2953	1.0113	−1.0792
.9569	1.3401	1.1207	−1.0754
1.0586	1.3802	1.2292	−1.0602
1.1618	1.4162	1.3354	−1.0335
1.2661	1.4488	1.4383	−.9960
1.3714	1.4784	1.5373	−.9492
1.4773	1.5053	1.6325	−.8949
1.5837	1.5299	1.7242	−.8350
1.6907	1.5526	1.8134	−.7714
1.7980	1.5733	1.9014	−.7061
1.9056	1.5923	1.9888	−.6401
2.0135	1.6097	2.0764	−.5743
2.1216	1.6255	2.1646	−.5093
2.2300	1.6399	2.2536	−.4453
2.3385	1.6527	2.3434	−.3826
2.4472	1.6641	2.4343	−.3214
2.5561	1.6740	2.5264	−.2621
2.6650	1.6825	2.6200	−.2051
2.7741	1.6896	2.7151	−.1507
2.8832	1.6954	2.8114	−.0985
2.9924	1.6998	2.9086	−.0479
3.1017	1.7029	3.0064	.0016
3.2110	1.7049	3.1048	.0496
3.3203	1.7056	3.2040	.0961
3.4295	1.7052	3.3040	.1409
3.5388	1.7037	3.4048	.1838
3.6481	1.7011	3.5065	.2247
3.7573	1.6975	3.6089	.2634
3.8665	1.6929	3.7122	.3002
3.9757	1.6873	3.8161	.3349

Upper surface		Lower surface	
$\frac{x}{c} \times 100$	$\frac{z}{c} \times 100$	$\frac{x}{c} \times 100$	$\frac{z}{c} \times 100$
4.0848	1.6807	3.9206	0.3678
4.1938	1.6733	4.0256	.3989
4.3028	1.6650	4.1311	.4287
4.4117	1.6560	4.2368	.4574
4.5206	1.6462	4.3428	.4854
4.6294	1.6356	4.4489	.5125
4.7381	1.6243	4.5553	.5384
4.8467	1.6124	4.6622	.5627
4.9553	1.5998	4.7695	.5850
5.0638	1.5865	4.8772	.6048
5.1722	1.5726	4.9854	.6223
5.2805	1.5579	5.0939	.6375
5.3887	1.5425	5.2026	.6508
5.4968	1.5265	5.3116	.6622
5.6048	1.5096	5.4207	.6718
5.7126	1.4921	5.5300	.6796
5.8204	1.4738	5.6394	.6858
5.9280	1.4547	5.7489	.6904
6.0355	1.4348	5.8584	.6936
6.1428	1.4142	5.9679	.6953
6.2500	1.3927	6.0775	.6956
6.3570	1.3705	6.1871	.6948
6.4638	1.3474	6.2966	.6927
6.5705	1.3235	6.4061	.6896
6.6769	1.2988	6.5156	.6855
6.7832	1.2732	6.6251	.6803
6.8892	1.2468	6.7345	.6744
6.9951	1.2196	6.8438	.6676
7.1007	1.1916	6.9531	.6599
7.2062	1.1629	7.0623	.6515
7.3115	1.1334	7.1715	.6423
7.4165	1.1034	7.2806	.6324
7.5214	1.0726	7.3896	.6217
7.6261	1.0413	7.4986	.6103
7.7307	1.0094	7.6075	.5982
7.8351	.9770	7.7163	.5855
7.9393	.9441	7.8251	.5722
8.0434	.9108	7.9338	.5583
8.1473	.8770	8.0424	.5438
8.2511	.8429	8.1509	.5287
8.3549	.8085	8.2593	.5131
8.4585	.7737	8.3677	.4970
8.5620	.7387	8.4760	.4804
8.6655	.7036	8.5842	.4633
8.7689	.6682	8.6924	.4458

Table A3. Concluded

Upper surface		Lower surface	
$\frac{x}{c} \times 100$	$\frac{z}{c} \times 100$	$\frac{x}{c} \times 100$	$\frac{z}{c} \times 100$
8.8723	0.6327	8.8005	0.4279
8.9756	.5971	8.9085	.4095
9.0789	.5613	9.0164	.3906
9.1821	.5255	9.1242	.3712
9.2854	.4895	9.2320	.3513
9.3886	.4535	9.3396	.3309
9.4917	.4175	9.4472	.3099
9.5949	.3814	9.5546	.2882
9.6980	.3453	9.6618	.2660
9.8026	.3086	9.7739	.2425

Table A4. Trailing-Edge Flap Coordinates

Upper surface		Lower surface	
$\frac{x}{c} \times 100$	$\frac{z}{c} \times 100$	$\frac{x}{c} \times 100$	$\frac{z}{c} \times 100$
0	0	0	0
.0646	.2603	.0590	−.2531
.1991	.4937	.2437	−.4372
.3722	.7004	.4869	−.5361
.5694	.8844	.7469	−.5762
.7836	1.0483	1.0103	−.5808
1.0093	1.1961	1.2735	−.5681
1.2421	1.3324	1.5365	−.5539
1.4800	1.4598	1.7998	−.5434
1.7225	1.5780	2.0631	−.5334
1.9693	1.6870	2.3264	−.5224
2.2201	1.7865	2.5896	−.5111
2.4745	1.8764	2.8528	−.5000
2.7323	1.9561	3.1161	−.4889
2.9929	2.0260	3.3793	−.4779
3.2559	2.0865	3.6426	−.4669
3.5206	2.1388	3.9058	−.4559
3.7865	2.1842	4.1691	−.4449
4.0533	2.2243	4.4324	−.4338
4.3208	2.2601	4.6956	−.4227
4.5887	2.2919	4.9588	−.4116
4.8571	2.3198	5.2221	−.4006
5.1259	2.3438	5.4853	−.3895
5.3949	2.3641	5.7486	−.3785
5.6642	2.3807	6.0118	−.3675
5.9338	2.3936	6.2751	−.3564
6.2034	2.4030	6.5384	−.3454
6.4732	2.4089	6.8016	−.3343
6.7430	2.4118	7.0649	−.3233
7.0128	2.4117	7.3282	−.3122
7.2826	2.4087	7.5914	−.3012
7.5524	2.4022	7.8547	−.2901
7.8220	2.3918	8.1180	−.2791
8.0914	2.3769	8.3812	−.2680
8.3605	2.3577	8.6445	−.2570
8.6293	2.3342	8.9078	−.2459
8.8977	2.3066	9.1710	−.2349
9.1658	2.2755	9.4343	−.2238
9.4335	2.2420	9.6975	−.2128
9.7011	2.2076	9.9608	−.2017
9.9688	2.1732	10.2241	−.1907
10.2365	2.1396	10.4874	−.1796
10.5043	2.1065	10.7507	−.1686
10.7721	2.0737	11.0139	−.1575

Upper surface		Lower surface	
$\frac{x}{c} \times 100$	$\frac{z}{c} \times 100$	$\frac{x}{c} \times 100$	$\frac{z}{c} \times 100$
11.0399	2.0409	11.2772	−0.1465
11.3078	2.0082	11.5405	−.1354
11.5756	1.9753	11.8037	−.1244
11.8434	1.9423	12.0670	−.1133
12.1112	1.9093	12.3303	−.1023
12.3790	1.8761	12.5935	−.0912
12.6467	1.8429	12.8568	−.0802
12.9145	1.8097	13.1201	−.0692
13.1823	1.7766	13.3833	−.0581
13.4501	1.7435	13.6466	−.0471
13.7179	1.7104	13.9099	−.0360
13.9857	1.6773	14.1731	−.0250
14.2535	1.6443	14.4364	−.0139
14.5213	1.6112	14.6997	−.0029
14.7890	1.5781	14.9630	.0082
15.0568	1.5450	15.2262	.0192
15.3246	1.5119	15.4895	.0303
15.5923	1.4789	15.7527	.0413
15.8601	1.4458	16.0159	.0524
16.1279	1.4127	16.2792	.0635
16.3956	1.3796	16.5424	.0746
16.6633	1.3466	16.8057	.0857
16.9311	1.3135	17.0689	.0966
17.1988	1.2804	17.3322	.1075
17.4666	1.2473	17.5954	.1180
17.7343	1.2142	17.8587	.1282
18.0021	1.1811	18.1220	.1379
18.2699	1.1480	18.3853	.1471
18.5377	1.1149	18.6487	.1556
18.8054	1.0818	18.9121	.1633
19.0732	1.0488	19.1755	.1702
19.3409	1.0157	19.4388	.1764
19.6087	.9826	19.7022	.1817
19.8765	.9495	19.9657	.1862
20.1442	.9165	20.2292	.1900
20.4120	.8834	20.4927	.1930
20.6797	.8503	20.7562	.1952
20.9475	.8172	21.0197	.1967
21.2153	.7841	21.2832	.1974
21.4830	.7511	21.5467	.1973
21.7508	.7180	21.8102	.1966
22.0185	.6849	22.0737	.1950
22.2863	.6518	22.3371	.1928
22.5540	.6187	22.6005	.1898
22.8218	.5857	22.8639	.1861

Table A4. Concluded

Upper surface		Lower surface	
$\frac{x}{c} \times 100$	$\frac{z}{c} \times 100$	$\frac{x}{c} \times 100$	$\frac{z}{c} \times 100$
23.0896	.5526	23.1274	0.1817
23.3573	.5195	23.3909	.1766
23.6251	.4864	23.6542	.1708
23.8929	.4533	23.9177	.1644
24.1606	.4203	24.1811	.1574
24.4284	.3872	24.4444	.1498
24.6961	.3541	24.7078	.1414
24.9639	.3210	24.9711	.1323
25.2316	.2880	25.2344	.1225
25.4994	.2549	25.4977	.1121
25.7726	.2211	25.7716	.1011

Appendix B

Force and Acceleration Equations

Symbols

The following parameters are illustrated in sketch A.

g	acceleration due to gravity ($1g \approx 32.174$ ft/sec^2)
$h_{i=1-4}$	horizontal load cell readings, lb
$l_{i=1-4}$	longitudinal acceleration, g units
$n_{i=1-4}$	vertical acceleration, g units
$v_{i=1-4}$	vertical load cell readings, lb
W	weight of wing, lb
x, y, z	Cartesian coordinate system measured from wing center of gravity
$\dot{\theta}$	pitch rate, rad/sec
$\dot{\phi}$	roll rate, rad/sec
$\dot{\psi}$	yaw rate, rad/sec

Dots over symbols denote derivatives with respect to time.
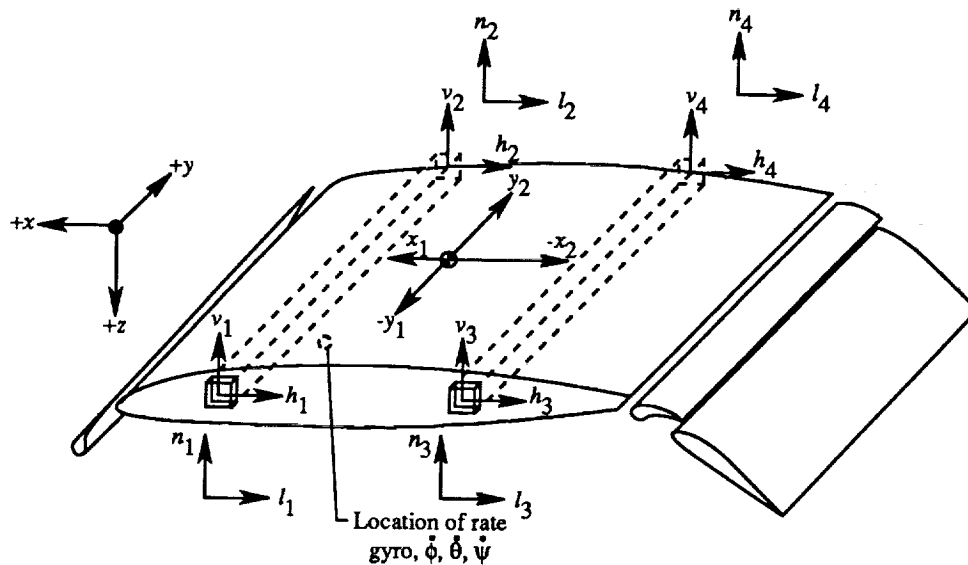
Sketch A

Force Equations

The required quantities of lift and drag are calculated by the following equations based on the wing geometry shown in sketch A.

The lift force equation is expressed as

$$\text{Lift} = v_1 + v_2 + v_3 + v_4 + W + \text{ Factor } L \tag{B1}$$

$$\text{Factor } L = \frac{W}{g}\left(\frac{n_1 + n_2 + n_3 + n_4}{4} - M - N + O\right) \tag{B2}$$

where

$$M = \frac{1}{2}\left(\dot{\phi}\dot{\psi} - \ddot{\theta}\right)(x_1 - x_2)$$

$$N = \frac{1}{2}\left(\dot{\theta}\dot{\psi} - \ddot{\phi}\right)(y_2 - y_1)$$

$$O = \frac{1}{2}\left(\dot{\phi}^2 + \dot{\theta}^2\right)(z_1 - z_2)$$

The drag force equation is written as

$$\text{Drag} = h_1 + h_2 + h_3 + h_4 + \text{ Factor } D \tag{B3}$$

$$\text{Factor } D = -\frac{W}{g}\left(\frac{l_1 + l_2 + l_3 + l_4}{4} - M' - N' + O'\right) \tag{B4}$$

where

$$M' = \frac{1}{2}\left(\dot{\theta}^2 + \dot{\psi}^2\right)(x_1 - x_2)$$

$$N' = \frac{1}{2}\left(\dot{\phi}\dot{\theta} - \ddot{\psi}\right)(y_2 - y_1)$$

$$O' = \frac{1}{2}\left(\dot{\phi}\dot{\psi} - \ddot{\theta}\right)(z_1 - z_2)$$

Acceleration Equations

The pitch acceleration equation is given as

$$\ddot{\theta} = \dot{\psi}\dot{\phi} + \left(\frac{z_1 + z_2}{x_1 + x_2}\right)\left(\dot{\phi}^2 + \dot{\theta}^2\right) - \frac{n_1 - n_2}{x_1 - x_2} \tag{B5}$$

the roll acceleration equation is given as

$$\ddot{\phi} = -\dot{\theta}\dot{\psi} + \frac{n_3 - n_1}{y_1 + y_2} \tag{B6}$$

and the yaw acceleration equation is given as

$$\ddot{\psi} = \frac{d\dot{\psi}}{dt} \tag{B7}$$

where t denotes the derivative of time.

The Factor terms L and D are required to take into account the forces that are exerted on the wing model as measured by the accelerometers and rate gyros. Nevertheless, preliminary checkout runs showed that these vibratory forces were of high frequency and that their effect on the aerodynamic lift data was negligible as shown in figure B1. The accelerometer data, which were filtered with a cut-off frequency of 1/2 Hz to remove the structural vibrations, are shown for the time period corresponding to the acquisition of aerodynamic data (approximately between 3 and 8 sec). This filtering removed the small contributions of Factor L from the lift equation; however, the net deceleration loads are large and must be accounted for in the drag equation with Factor D. The resultant net drag force is the difference between the inertial and longitudinal aerodynamic forces. This small difference between two large numbers yields unreliable drag measurements, and therefore drag data are not

presented. Refinements to the drag measuring technique are being investigated. The above derived equations are consistent with the method presented in reference B1.

Reference

B1. Gainer, Thomas G.; and Hoffman, Sherwood: *Summary of Transformation Equations and Equations of Motion Used in Free-Flight and Wind-Tunnel Data Reduction and Analysis.* NASA SP-3070, 1972.
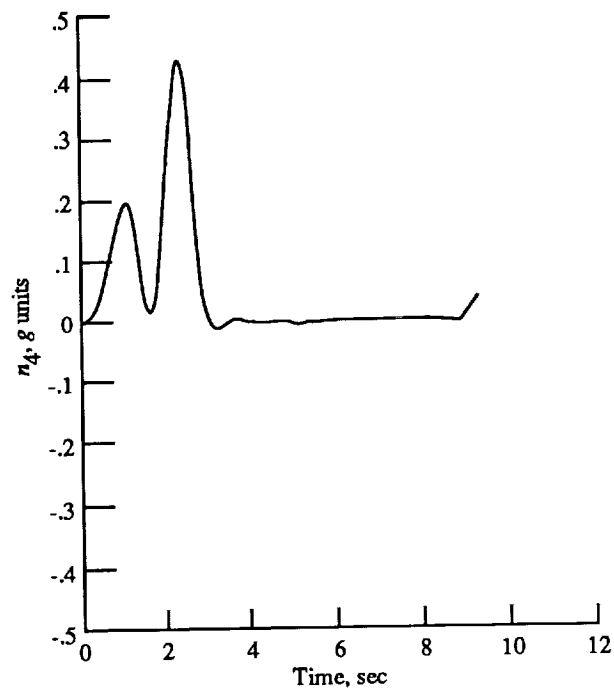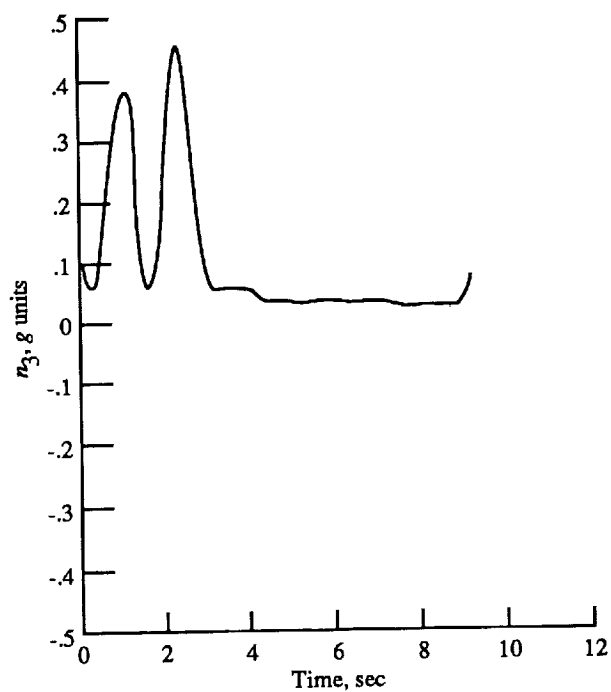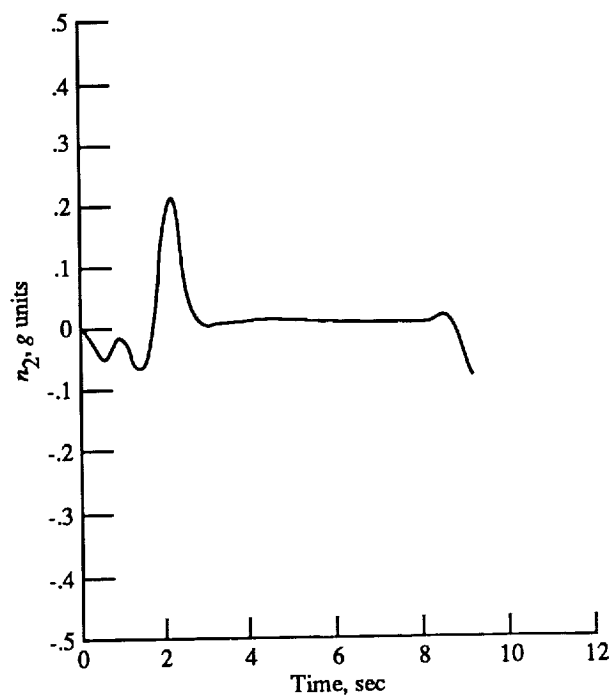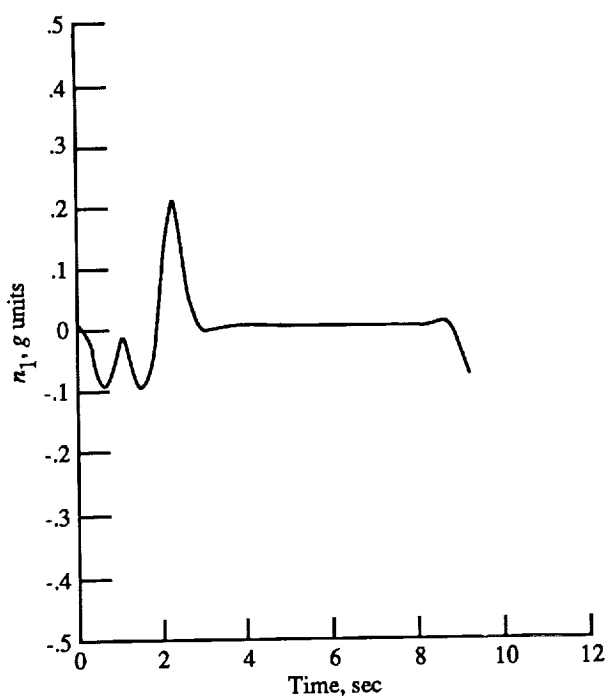
(a) Vertical acceleration data filtered at 0.5 Hz during 160-knot test run.

Figure B1. Vibratory forces measured by accelerometer and rate gyro.
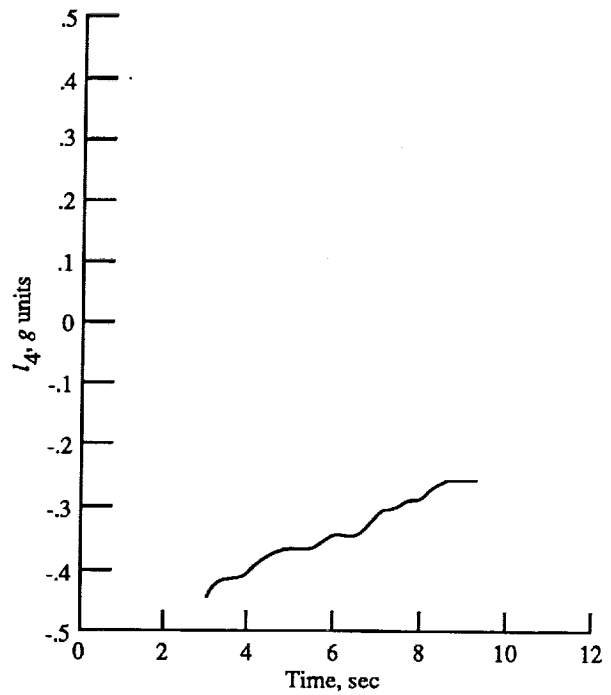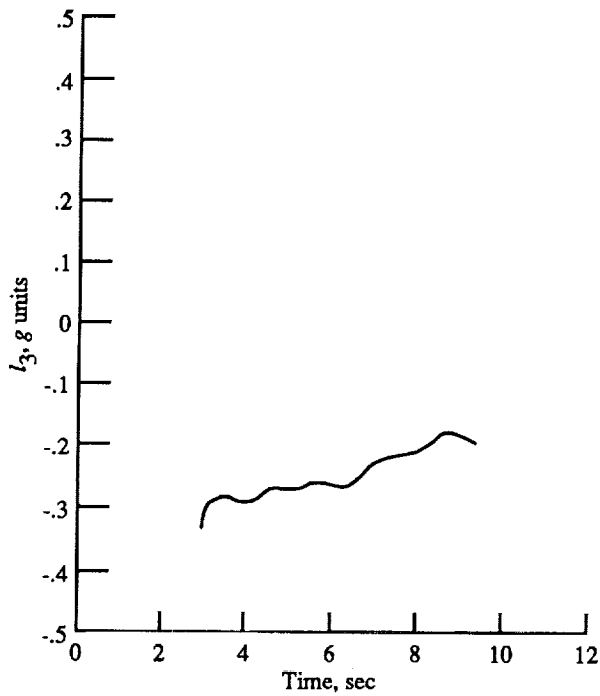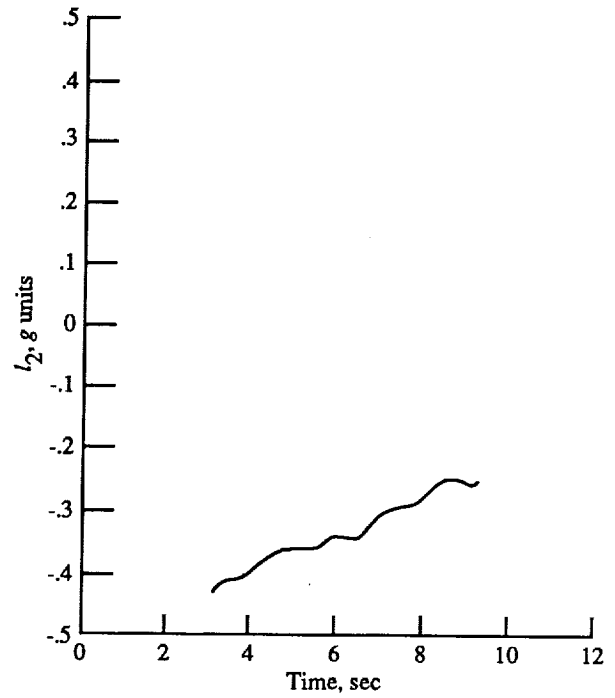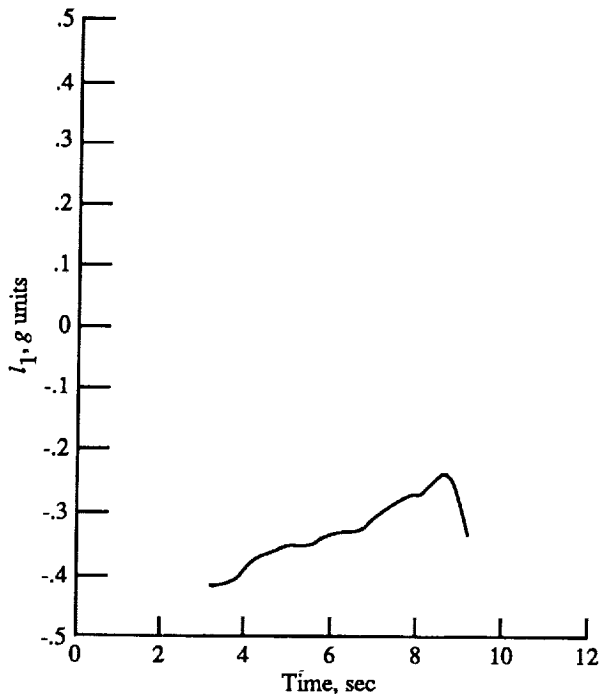
(b) Longitudinal acceleration data filtered at 0.5 Hz during 160-knot test run.

Figure B1. Continued.
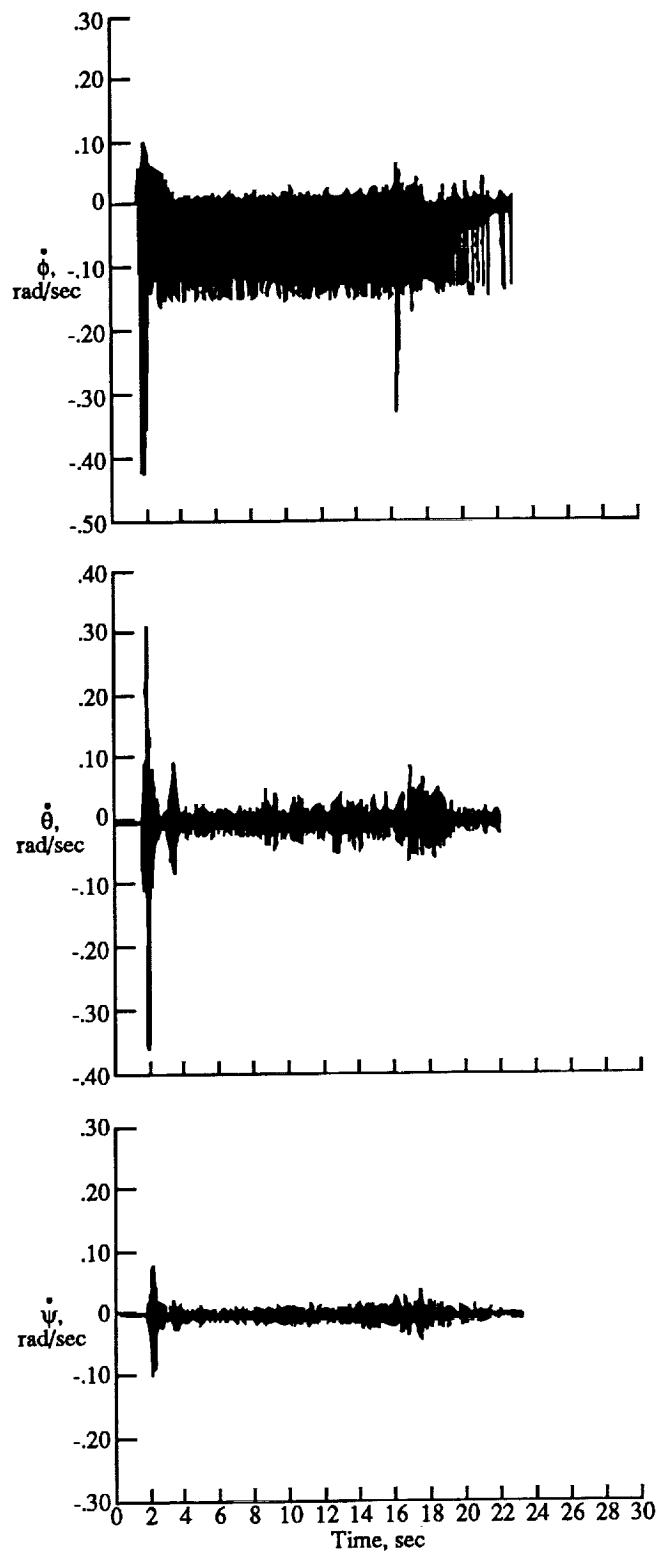
(c) Roll, pitch, and yaw rate data filtered at 200 Hz during 100-knot test run.

Figure B1. Concluded.

References

1. *Low-Altitude Wind Shear and Its Hazard to Aviation.* National Academy Press, 1983.

2. Joss, J.; and Waldvogel, A.: Raindrop Size Distribution and Sampling Size Errors. *J. Atmos. Sci.,* vol. 26, no. 3, May 1969, pp. 566–569.

3. Markowitz, Allan H.: Raindrop Size Distribution Expressions. *J. Appl. Meteorol.,* vol. 15, no. 9, Sept. 1976, pp. 1029–1031.

4. Roys, George P.; and Kessler, Edwin: *Measurements by Aircraft of Condensed Water in Great Plains Thunderstorms.* Tech. Note 49-NSSP-19, U.S. Dep. of Commerce, July 1966.

5. Melson, W. E., Jr.: Observation and Comparison of Rainfall Measured at a High Sample Rate. *Preprints— Seventh Symposium on Meteorological Observations and Instrumentations,* American Meteorological Soc., 1991, pp. 195 198.

6. Rhode, Richard V.: *Some Effects of Rainfall on Flight of Airplanes and on Instrument Indications.* NACA TN 803, 1941.

7. Haines, P. A.; and Luers, J. K.: *Aerodynamic Penalties of Heavy Rain on Landing Aircraft.* NASA CR-156885, 1982.

8. Dunham, R. E., Jr.: Potential Influences of Heavy Rain on General Aviation Airplane Performance. AIAA-86-2606, Sept.-Oct. 1986.

9. Bezos, Gaudy M.; Dunham, R. Earl, Jr.; Gentry, Garl L., Jr.; and Melson, W. Edward, Jr.: *Wind Tunnel Aerodynamic Characteristics of a Transport-Type Airfoil in a Simulated Heavy Rain Environment.* NASA TP-3184, 1992.

10. Hansman, R. John, Jr.; and Barsotti, Martitia F.: The Aerodynamic Effect of Surface Wetting Characteristics on a Laminar Flow Airfoil in Simulated Heavy Rain. AIAA-85-0260, Jan. 1985.

11. Hansman, R. John, Jr.; and Craig, Anthony P.: Comparative Low Reynolds Number Tests of NACA 64-210, NACA 0012, and Wortmann FX67-K170 Airfoils in Heavy Rain. AIAA-87-0259, Jan. 1987.

12. Campbell, Bryan A.; and Bezos, Gaudy M.: *Steady-State and Transitional Aerodynamic Characteristics of a Wing in Simulated Heavy Rain.* NASA TP-2932, 1989.

13. Bilanin, Alan J.: Scaling Laws for Testing of High Lift Airfoils Under Heavy Rainfall. AIAA-85-0257, Jan. 1985.

14. Davis, Pamela A.; Stubbs, Sandy M.; and Tanner, John A.: *Langley Aircraft Landing Dynamics Facility.* NASA RP-1189, 1987.

15. Hoerner, Sighard F.; and Borst, Henry V.: *Fluid-Dynamic Lift.* Hoerner Fluid Dynamics (Brick Town, New Jersey), c.1975.

16. Taylor, John T.; Moore, Cadd T., III; Campbell, Bryan A.; and Melson, W. Edward, Jr.: The Development of a Facility for Full-Scale Testing of Airfoil Performance in Simulated Rain. AIAA-88-0055, Jan. 1988.

17. Bilanin, A. J.; Quackenbush, T. R.; and Feo, A.: *Feasibility of Predicting Performance Degradation of Airfoils in Heavy Rain.* NASA CR-181842, 1989.

18. Rogers, J. S.; Johnson, L. C.; and Jones, D. M. A.: Sources of Error in Calculating the Kinetic Energy of Rainfall. *J. Soil & Water Conserv.,* vol. 22, no. 4, July–Aug. 1967, pp. 140–142.

19. Melson, W. Edward, Jr.: Heavy Rain Characteristics and Ground Measurement Comparisons. Paper presented at the WMO IAHS 8th International Workshop on Precipitation Measurement (St. Moritz, Switzerland), Dec. 4 7, 1989.

20. Marshall, J. S.; and Palmer, W. McK.: The Distribution of Raindrops With Size. *J. Meteorol.,* vol. 5, no. 4, Aug. 1948, pp. 165 166.

Table I. Description of Spray Nozzles

Nozzle		Liquid water content, g/m^3
Diameter (commercially available), in.	Spacing along track length,[a] ft	
1/4	8	2
1/2	6	9
1/2	2	26
3/4	2	35

[a]Lateral spacing of all nozzles is fixed at 7.5 ft.

Table II. Theoretical Vertical Drop Velocity

[Nozzle pressure, 6/10 psi; corresponding theoretical exit velocity, 29.856/39.37 ft/sec]

Drop diameter, mm	Velocity at 14 ft from nozzle, ft/sec	Terminal velocity, ft/sec
0.5	6.561/6.561	6.561
1.0	13.451/13.123	13.123
2.0	22.966/23.95	22.966
3.0	27.23/30.184	24.247
4.0	29.12/32.48	29.528

Table III. List of Measurements

Vertical forces	Two load cells, each rated to 20 000 lb Two load cells, each rated at 10 000 lb
Longitudinal forces	Four load cells, each calibrated to 3000 lb (Rated capacity = 10 000 lb)
Accuracy of load cells	0.1 percent of rated capacity
Vertical accelerations	Four accelerometers rated to $\pm 4g$ Accuracy = 0.01g Resolution of 0.002g
Longitudinal accelerations	Four accelerometers rated to $\pm 4g$ Accuracy = 0.01g Resolution = 0.002g
Pitch, roll, yaw rates	Range = -0.5 rad/sec to 5 rad/sec Accuracy = 0.01 rad/sec Resolution = 0.0005 rad/sec
Carriage velocity	75–170 knots
Dynamic pressure	Range = 0 to 1 psid Accuracy = 0.015 psid Resolution = 0.0002 psid
Discrete data at time of launch	Wind velocity, mph, and direction, deg Barometric pressure, in. Temperature, °F
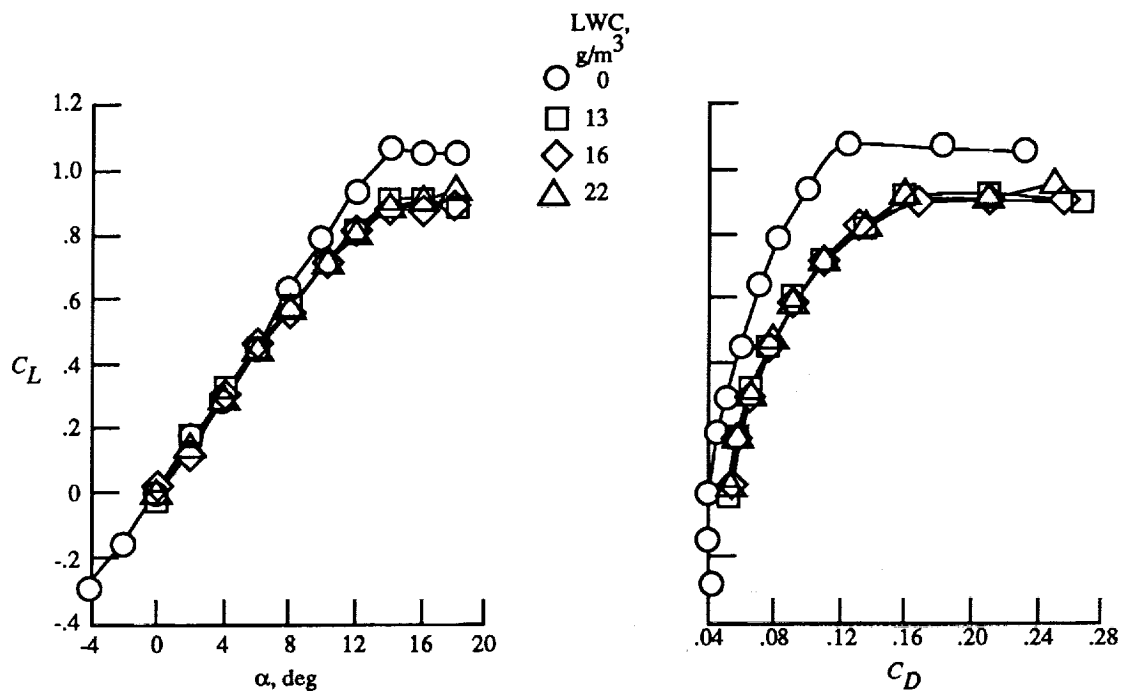
(a) Aerodynamics of cruise configuration.
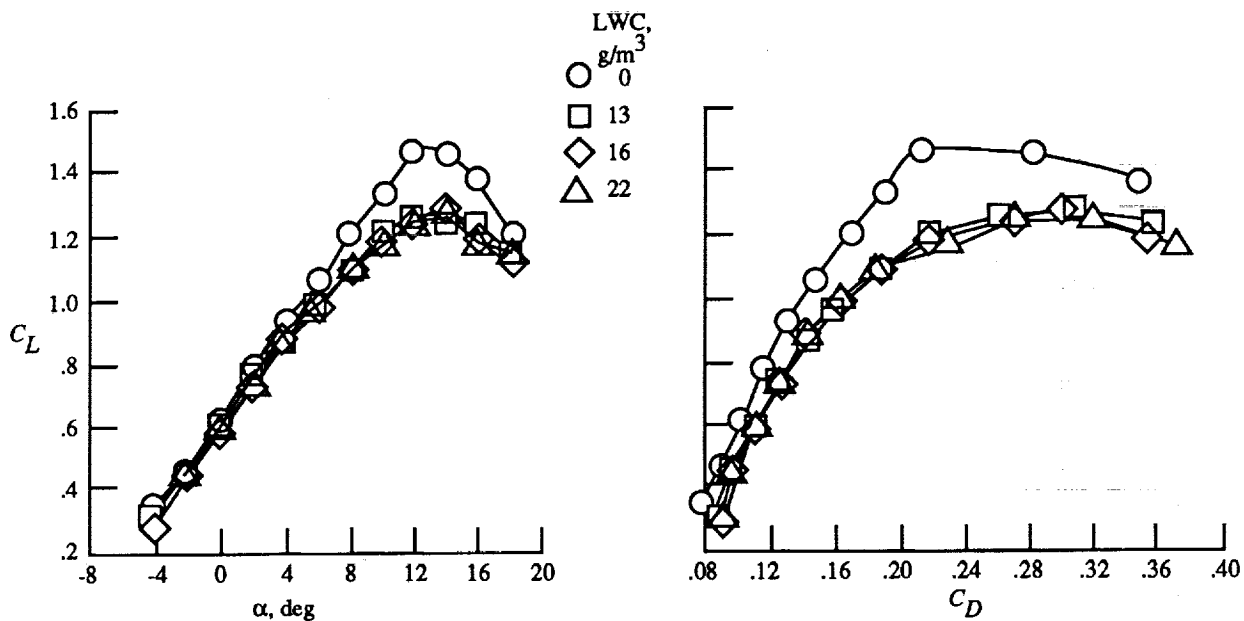
(b) Aerodynamics of high-lift configuration with 30-percent-chord flap deflected 20°.

Figure 1. Wind tunnel data on heavy rain effects obtained on NACA 0012 airfoil model at $q = 30$ psf and $N_{Re} = 1.7 \times 10^6$.
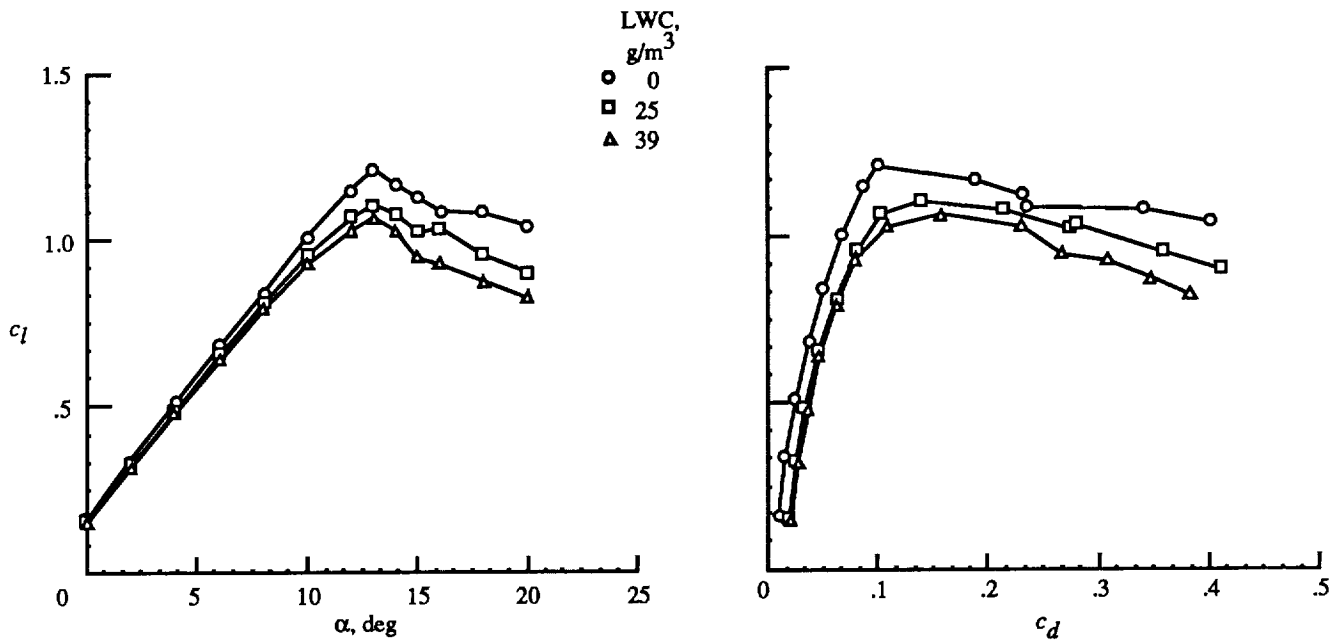
(a) Cruise configuration.
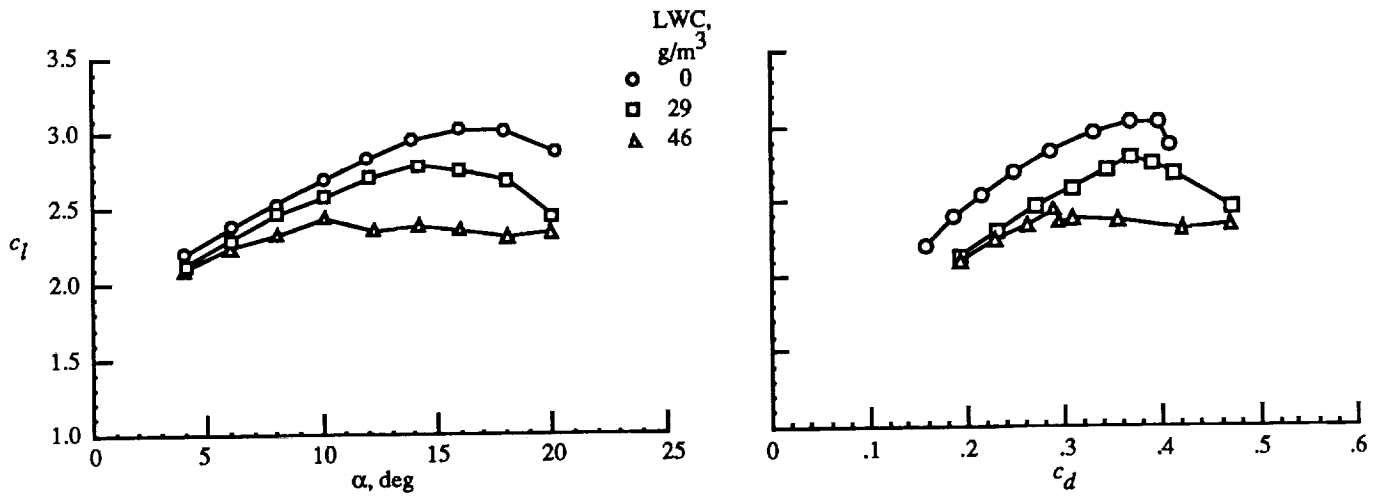
(b) Landing configuration.

Figure 2. Wind tunnel data on heavy rain effects obtained on NACA 64-210 airfoil model at $q = 30$ psf and $N_{Re} = 2.6 \times 10^6$.
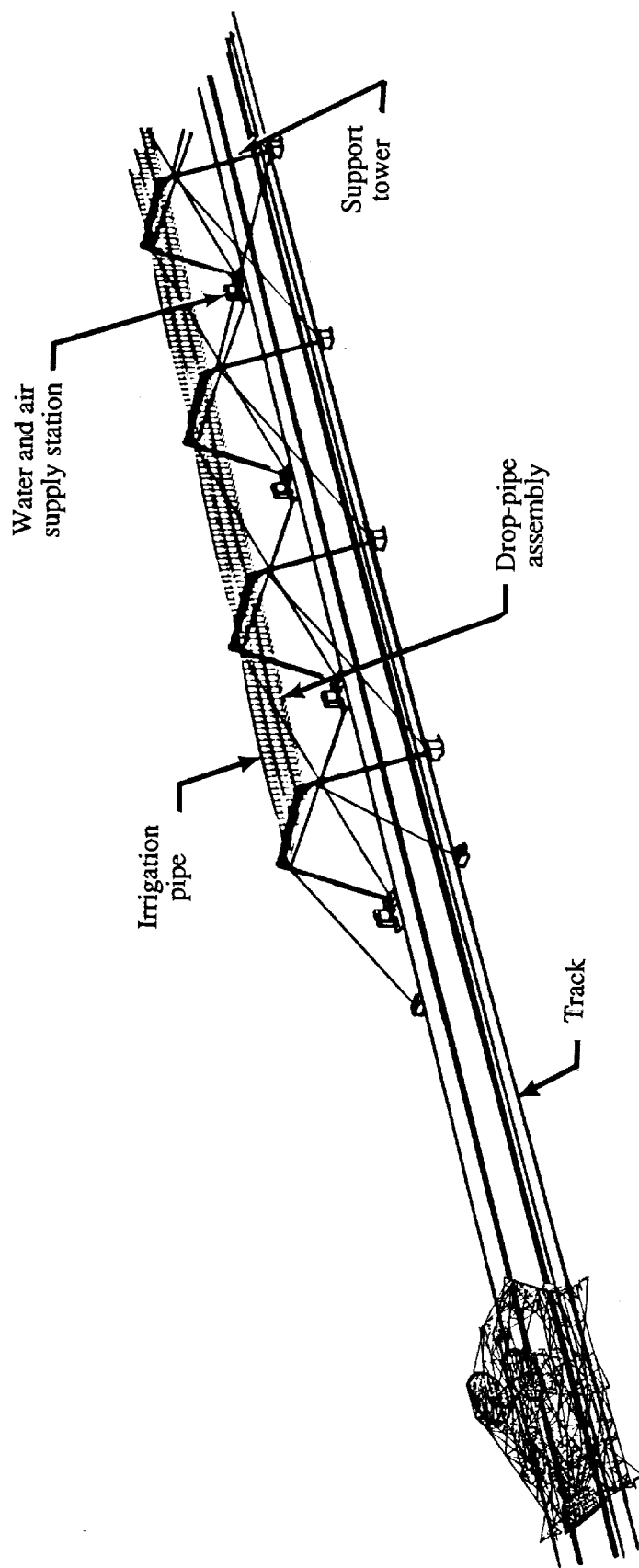
Figure 3. Illustration of large-scale testing technique developed to obtain aerodynamic data in simulated rain environment.

Support tower

Water and air supply station

Drop-pipe assembly

Irrigation pipe

Track

34
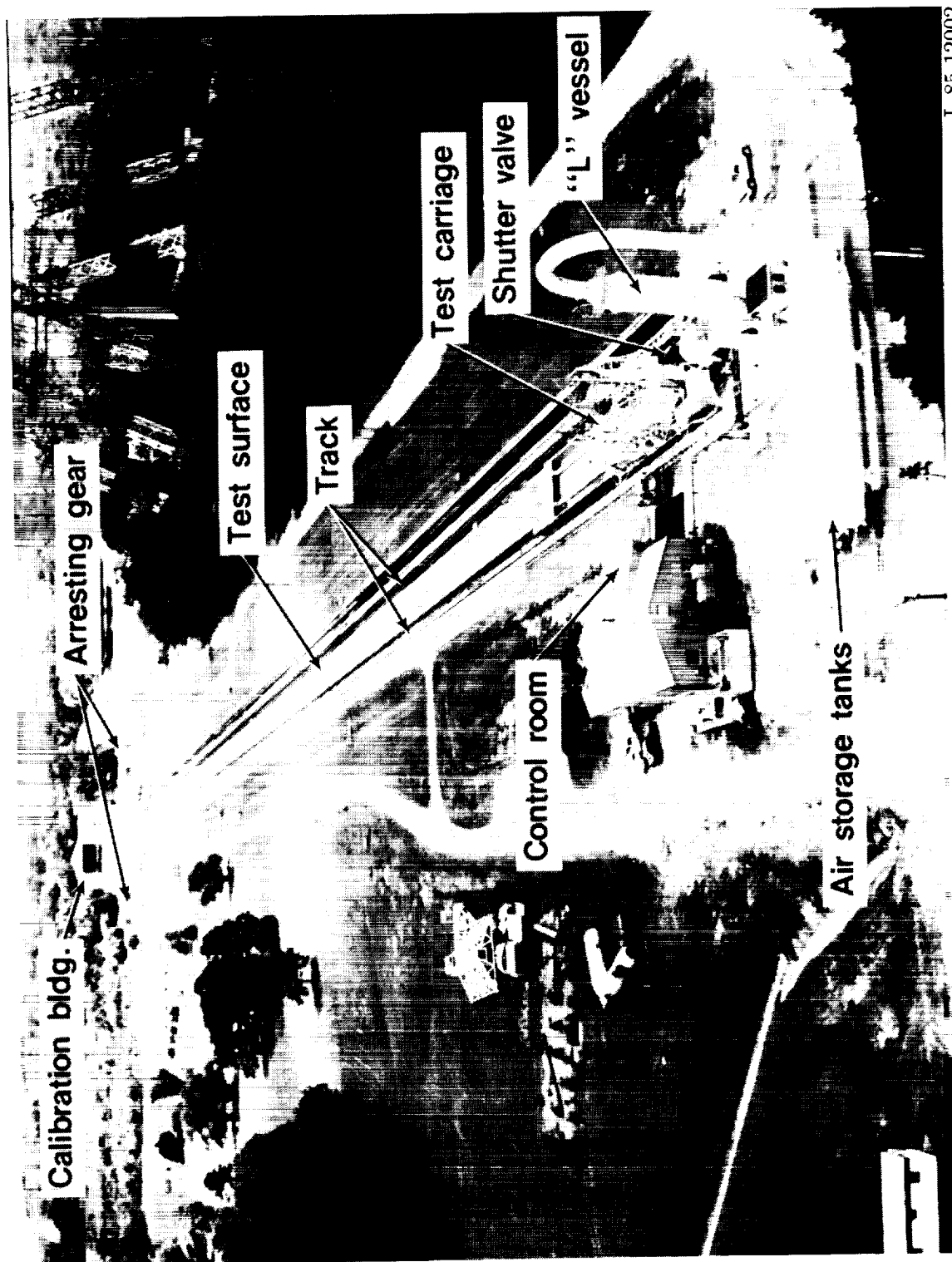
Figure 4. Aerial photograph of the Langley Aircraft Landing Dynamics Facility (ALDF) prior to heavy rain effects testing modifications.

L-85-12002

Figure 5. Aerial photograph of the ALDF test carriage prior to heavy rain effects testing modifications.

L-85-5330

36
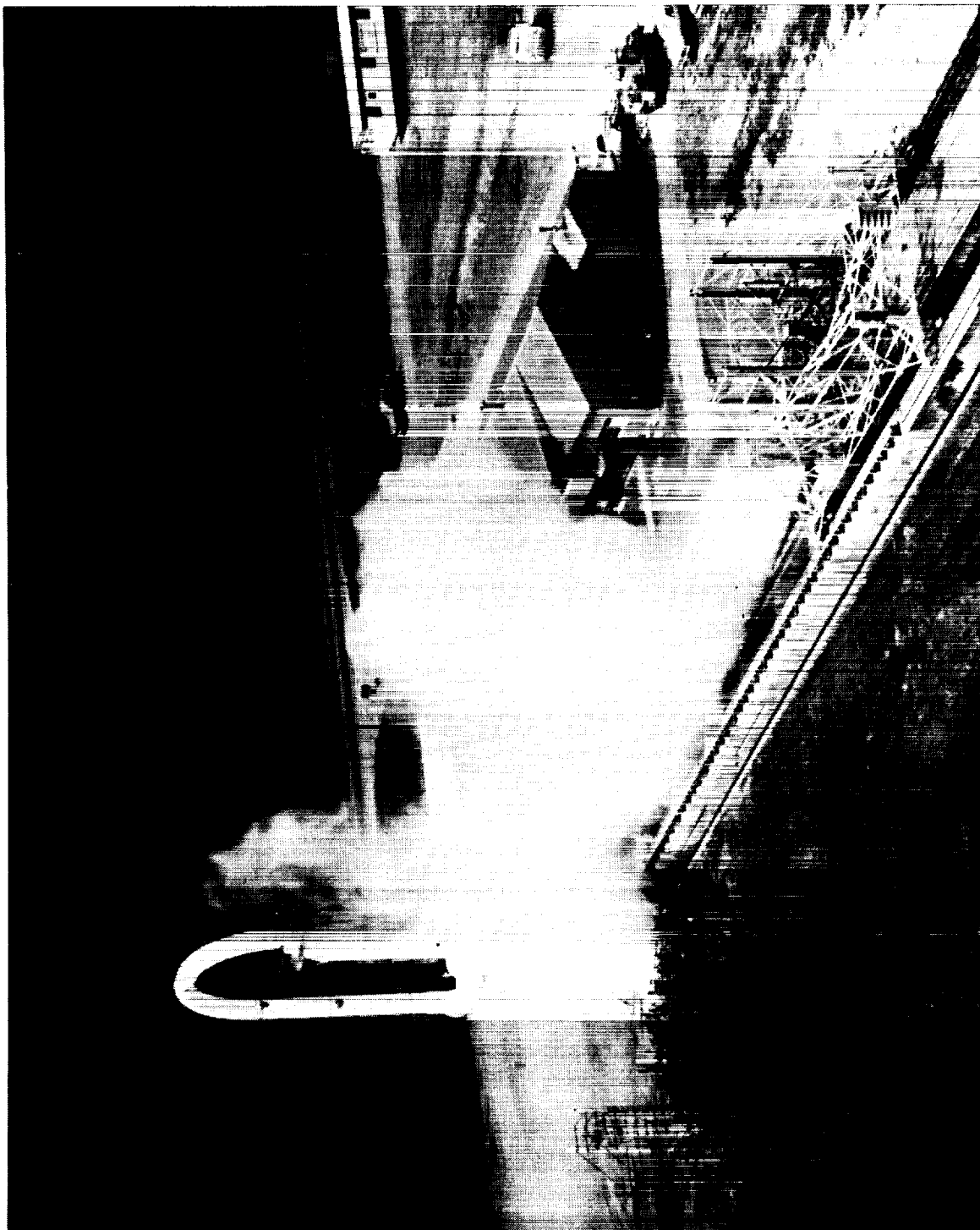
Figure 6. Aerial photograph of the ALDF test carriage during launch-acceleration phase of test run prior to heavy rain effects testing modifications.

L-86-50415
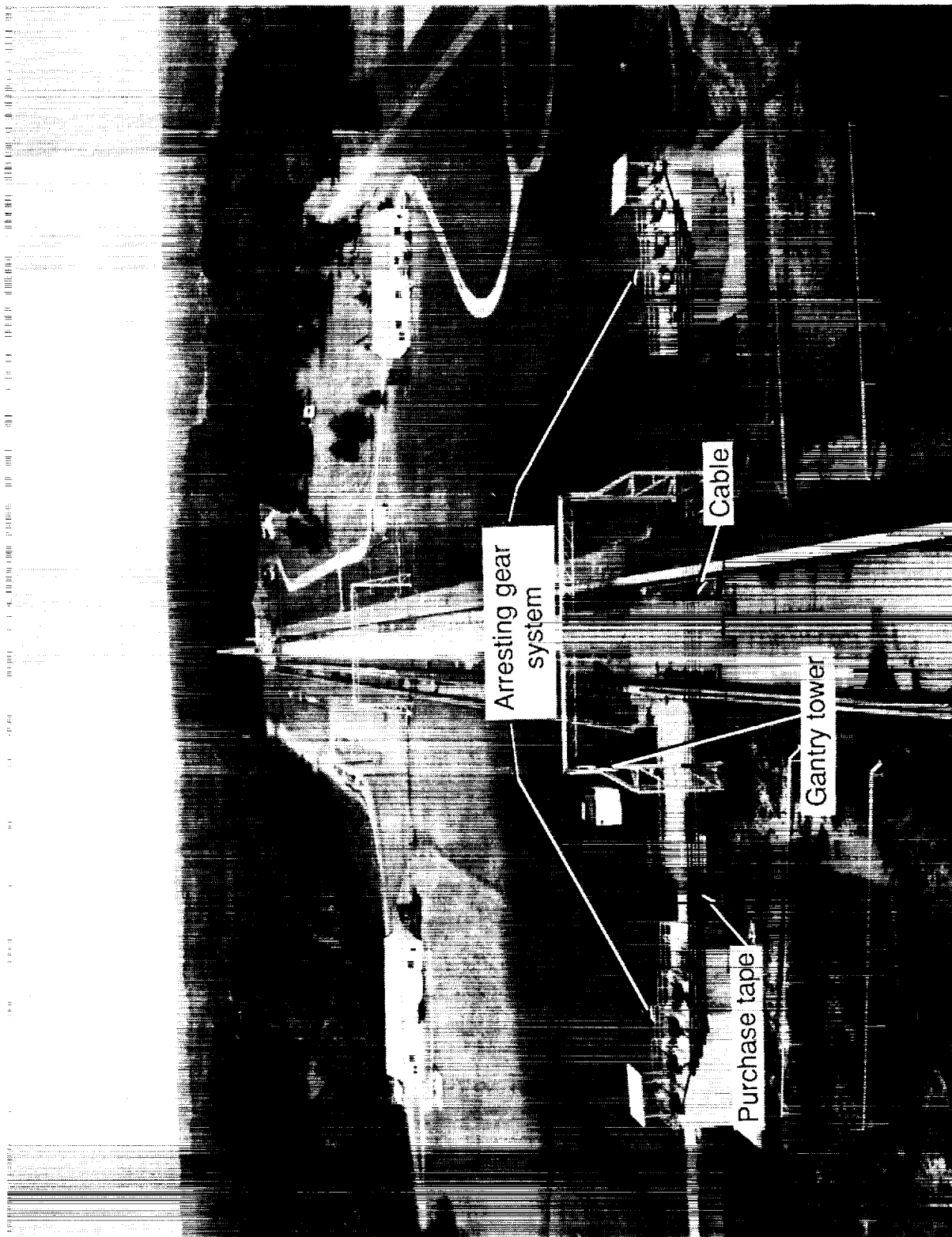
Figure 7. An aerial photograph of the ALDF arrestment system prior to heavy rain effects testing modifications.

L-87-649

ORIGINAL PAGE
BLACK AND WHITE PHOTOGRAPH
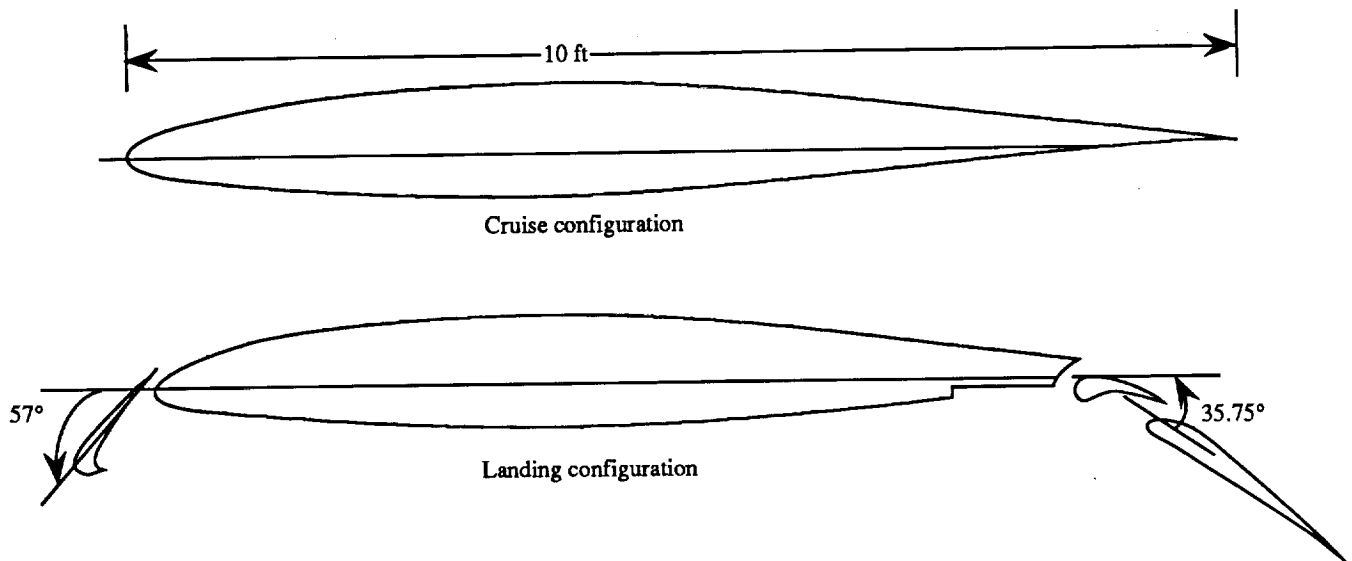
Figure 8. Cross section of an NACA 64-210 airfoil section and details of the model configurations.
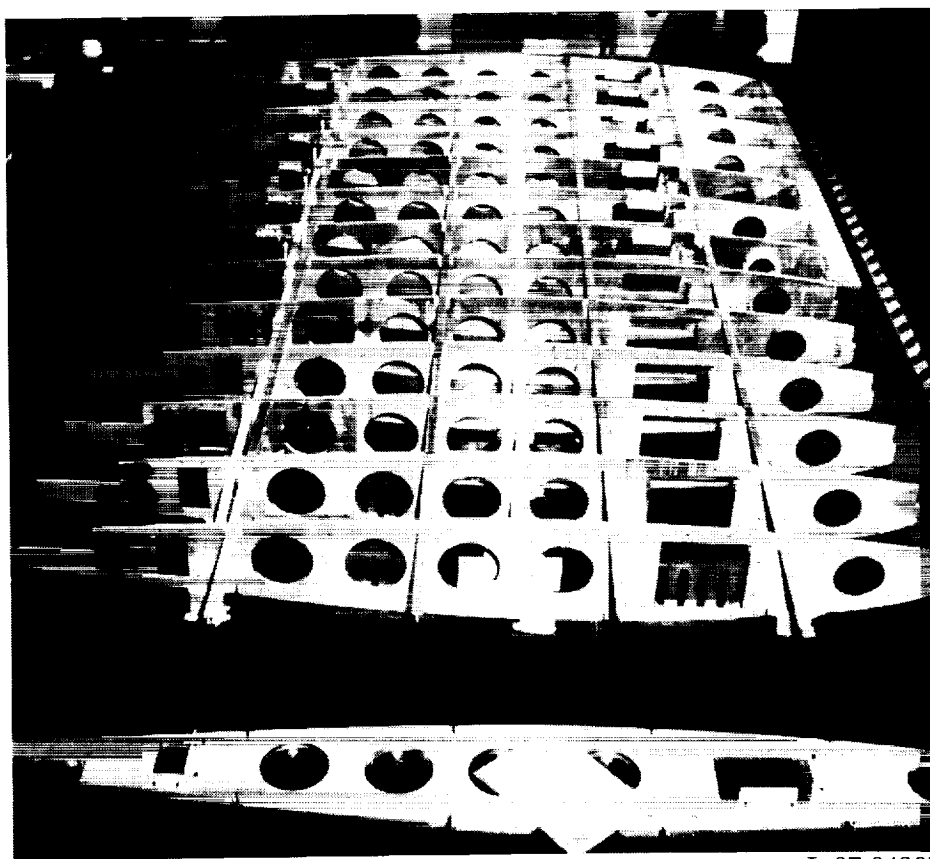
L-87-04365

Figure 9. View of the ALDF wing ribs under construction.
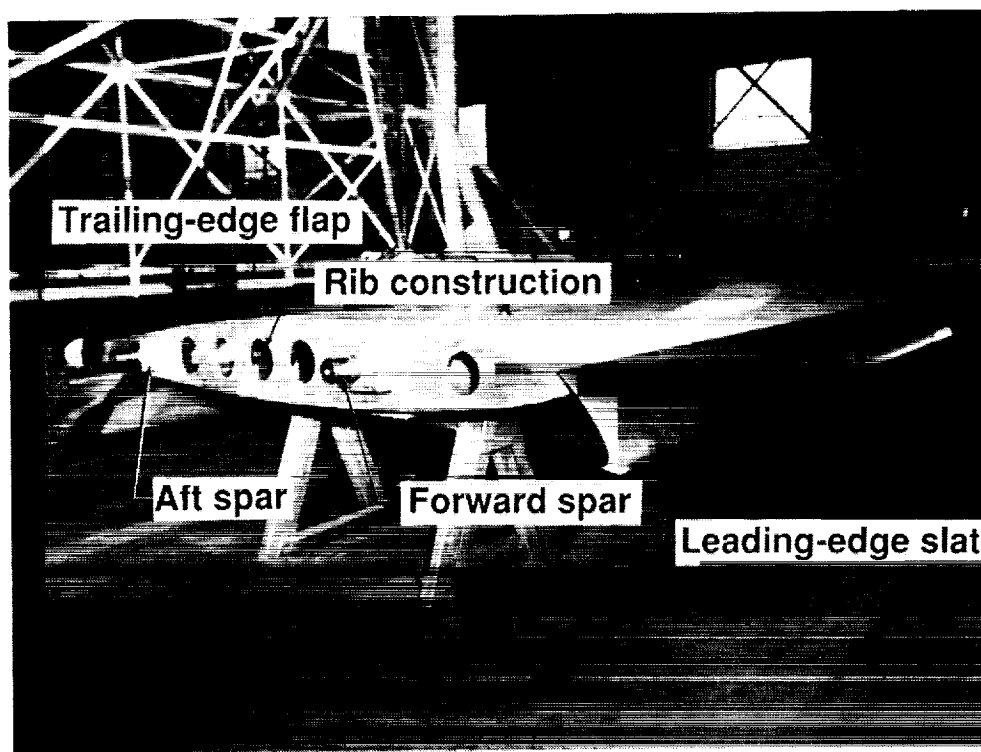
L-88-7178

(a) Front view.
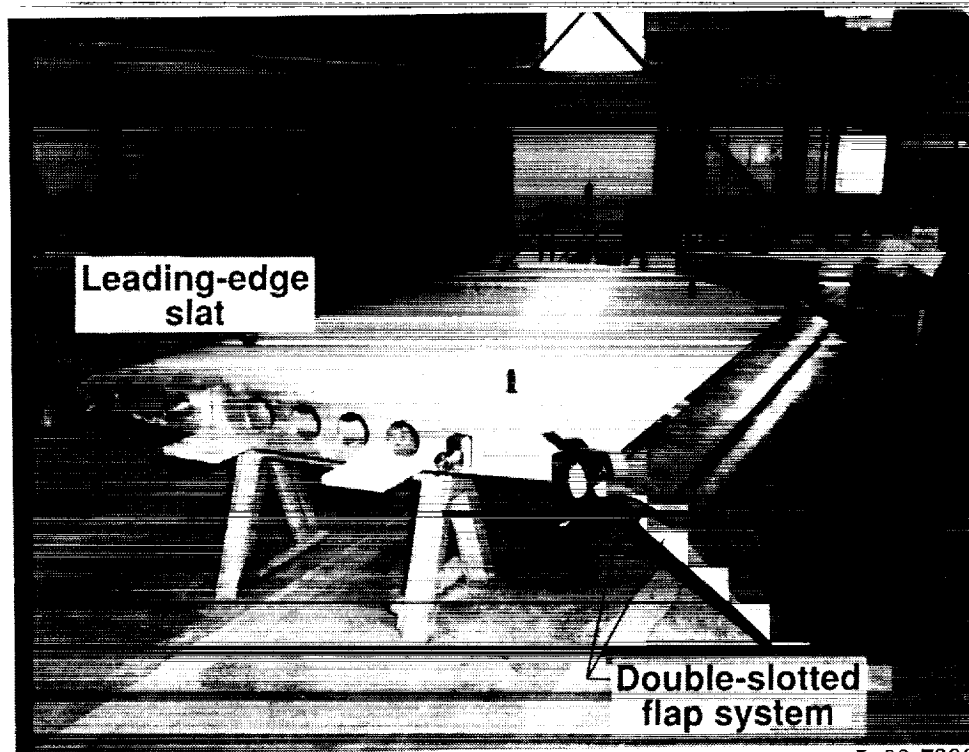
L-88-7396

(b) Aft view.

Figure 10. Views of the ALDF wing section in the landing configuration assembled before installation on the test carriage.
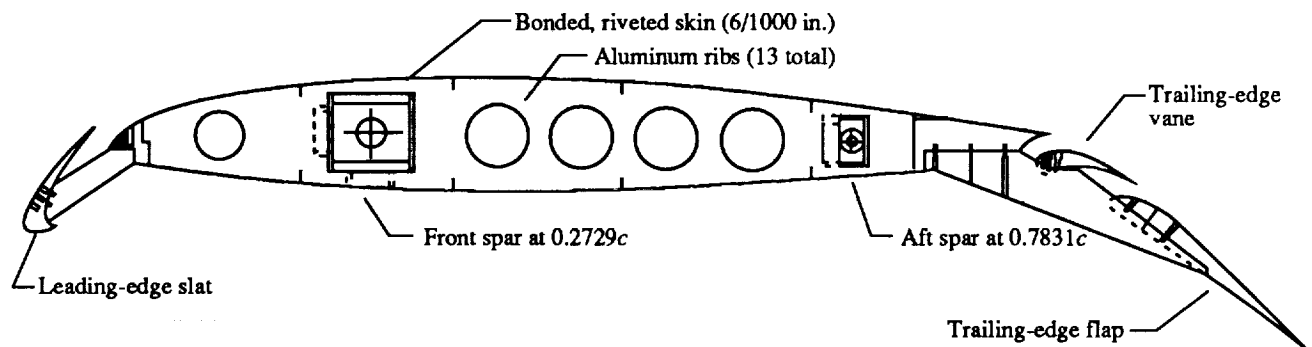
Figure 11. Details of the ALDF wing structure.
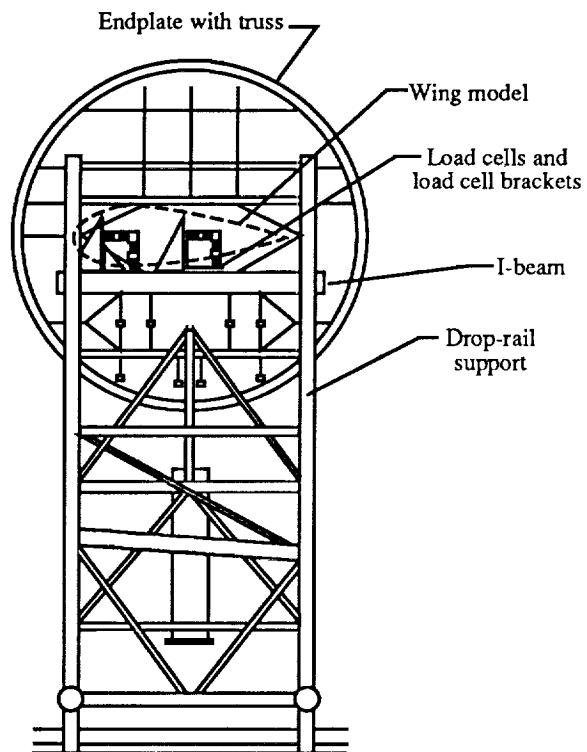
Figure 12. Details of location of the ALDF wing and load cell hardware with the test carriage structure omitted.

Figure 13. Closeup view of wing load-cell hardware and angle-of-attack mechanism of the ALDF.

L-88-08362
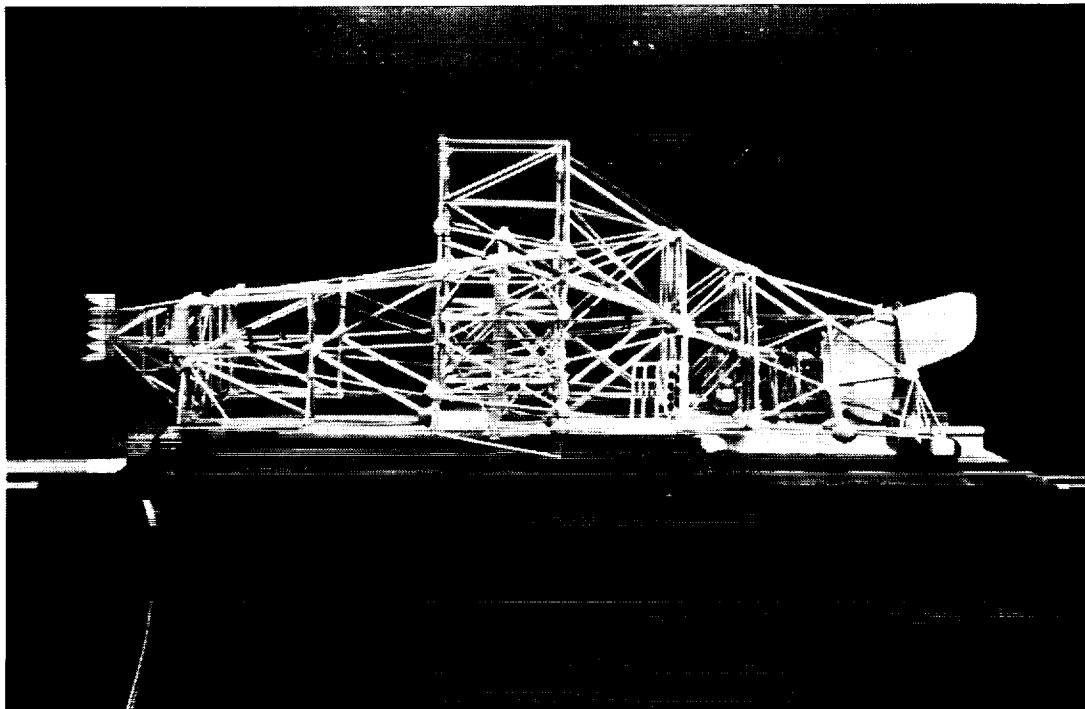
L-86-4745

Figure 14. View of 1/20th-scale model of the ALDF test carriage in the Langley 12-Foot Low-Speed Tunnel.
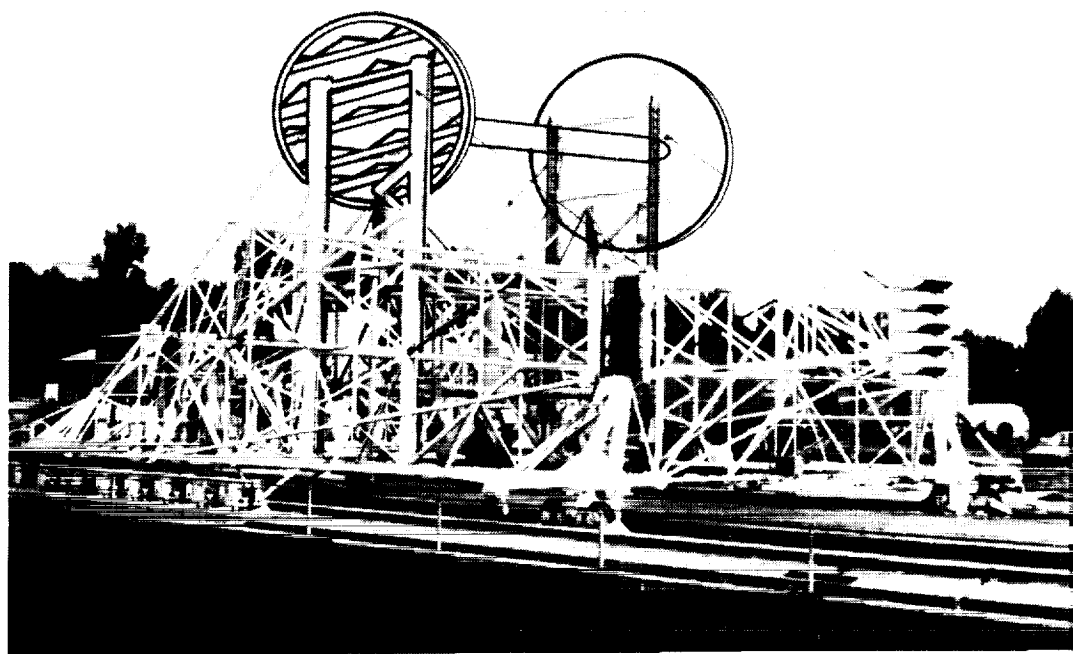
L-87-5529

Figure 15. Artist's sketch of proposed wing model location superimposed on the ALDF test carriage.

43
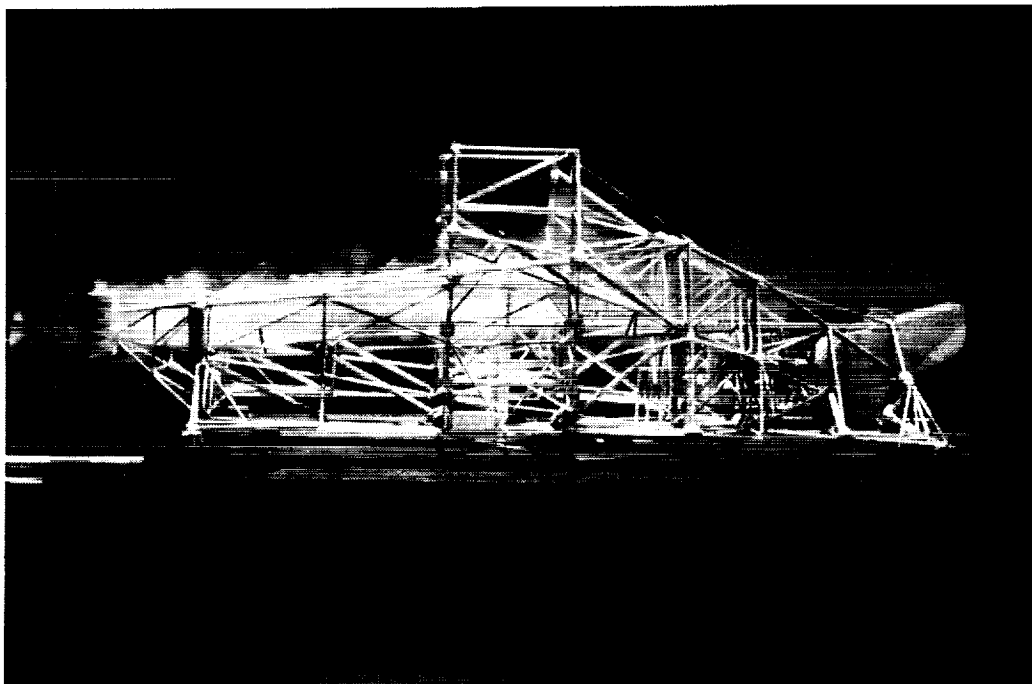
L-86-4650

Figure 16. Smoke visualization photograph of nose-block-induced airflow disturbances obtained on 1/20th-scale model of the ALDF test carriage in the Langley 12-Foot Low-Speed Tunnel at $q = 2$ psf.
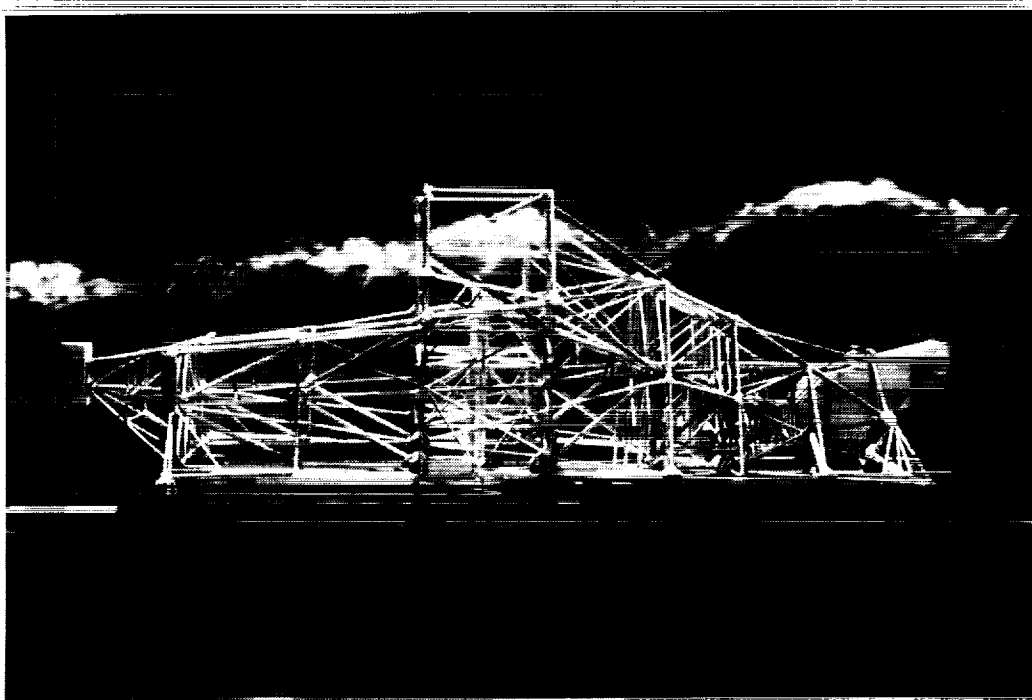
L-86-4645

Figure 17. Smoke visualization photograph of airflow at proposed wing model location of 1/20th-scale model of the ALDF test carriage obtained in the Langley 12-Foot Low-Speed Tunnel at $q = 2$ psf.

44

Figure 18. Side view of 40-in/hr rain field in front of the ALDF wing during 160-knot test run.

L-88-12310

45
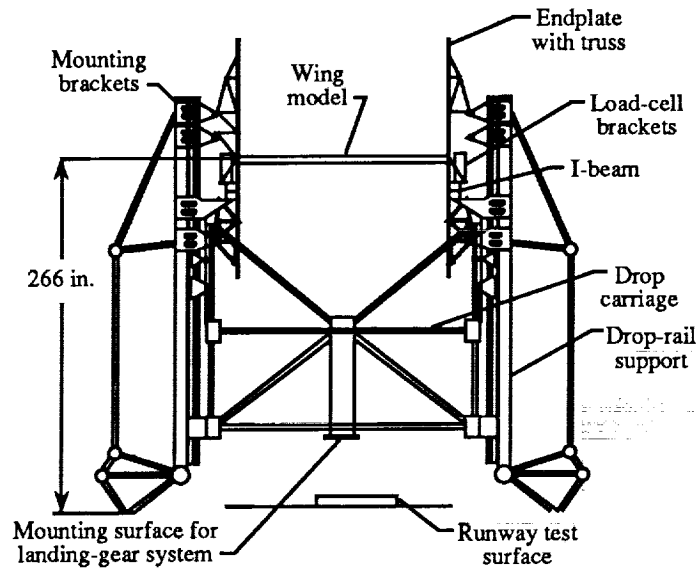
Figure 19. Details of front view of the ALDF test carriage with wing, endplates, and support structure mounted.
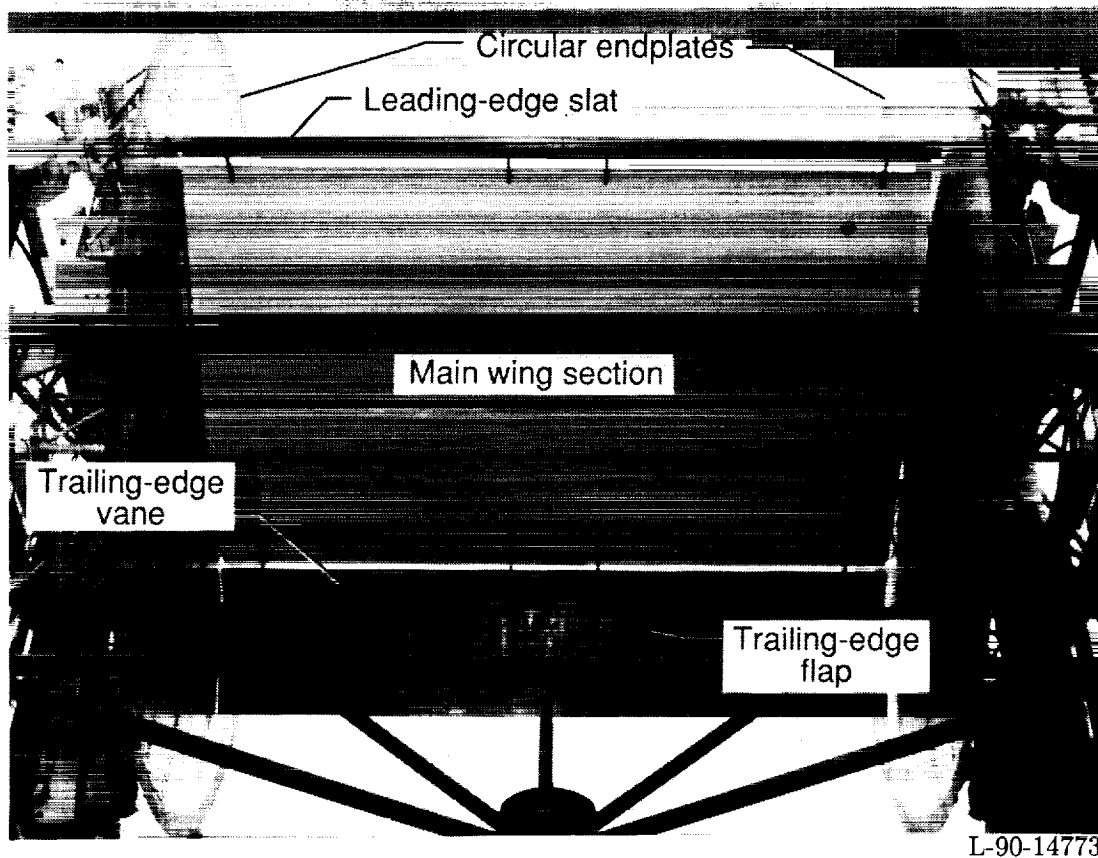
L-90-14773

Figure 20. Underside view of wing hardware installed on the ALDF test carriage at $\alpha = 18°$.
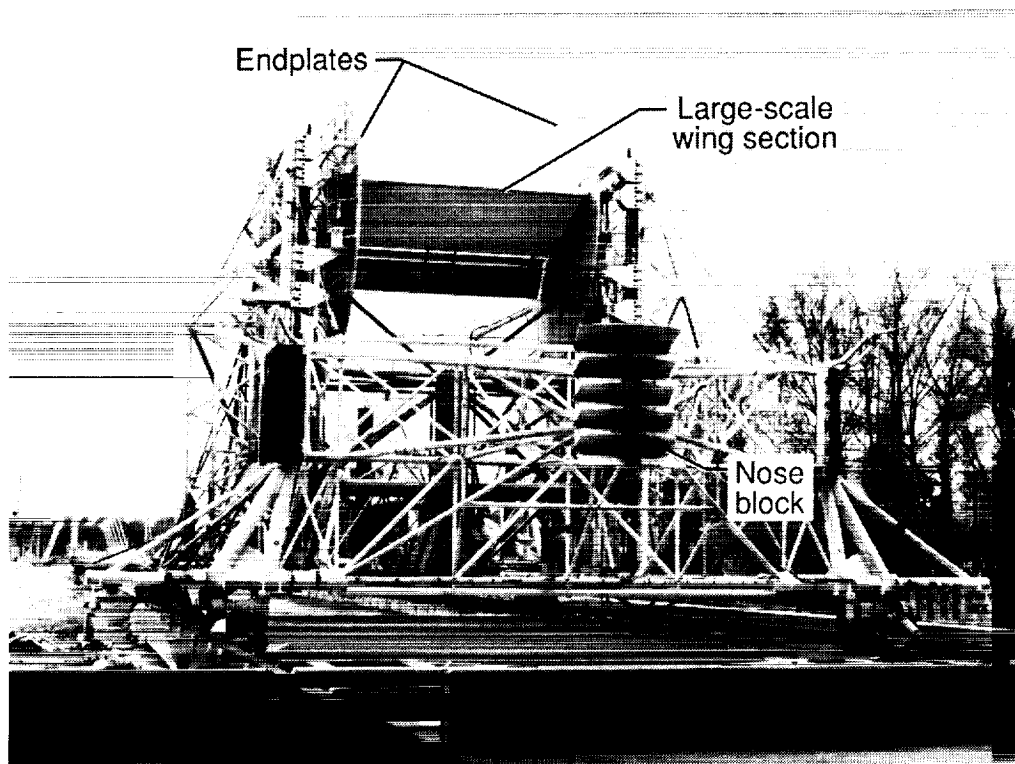
(a) Front view.
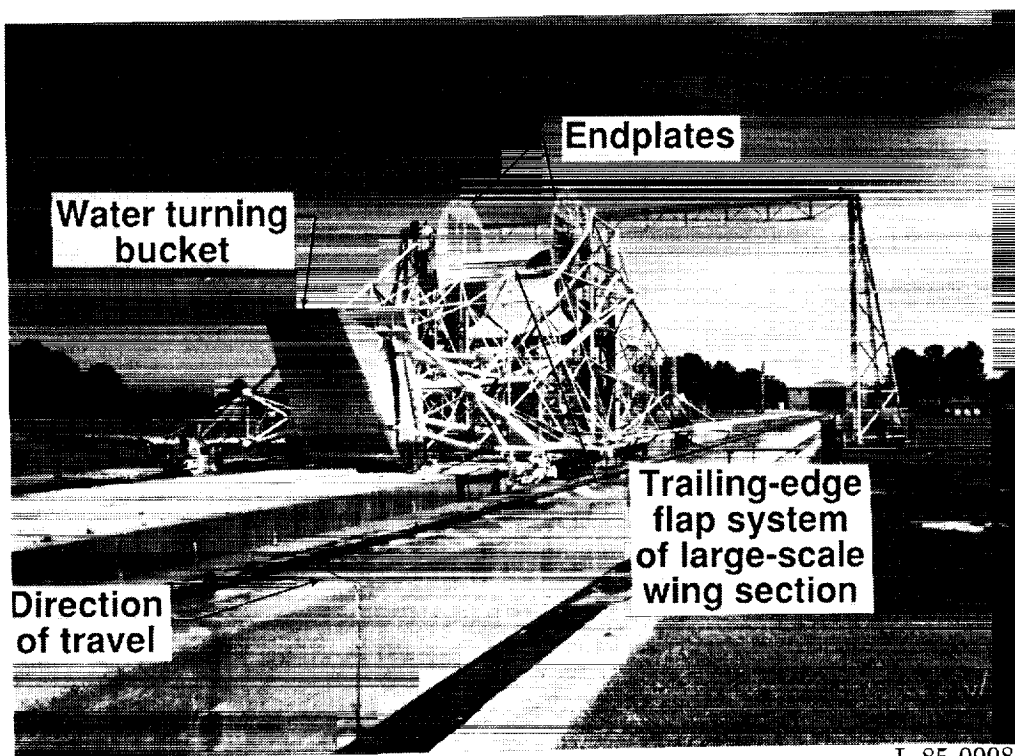
(b) Aft view.

Figure 21. Views of modified ALDF test carriage equipped with wing hardware, endplates, and support structure.
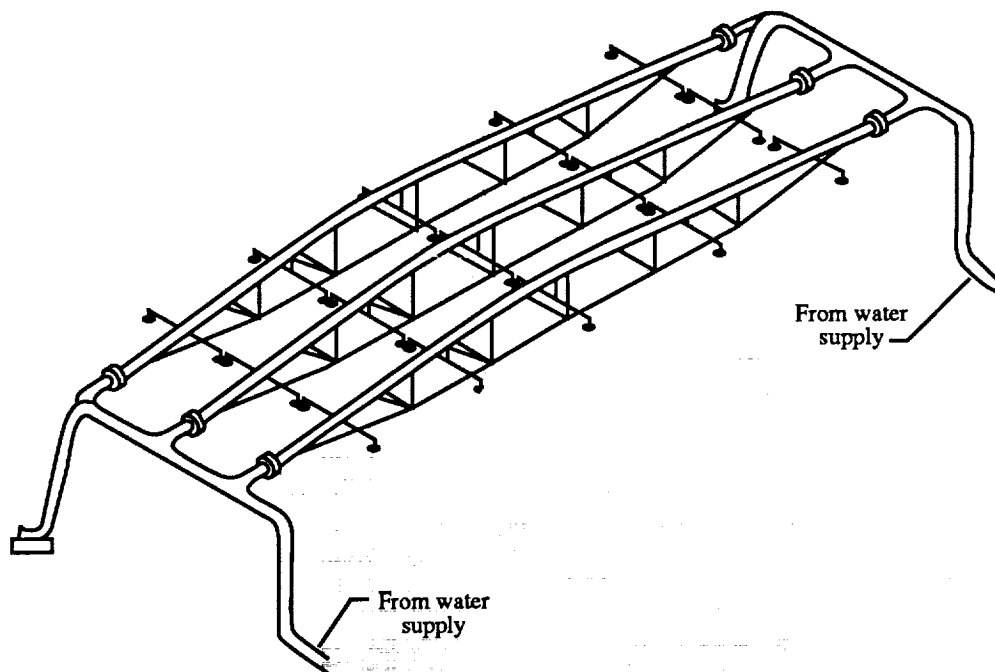
Figure 22. Illustration of the ALDF RSS concept.

WI-504-11

Figure 23. Photograph of prototype rain simulation system tested at the NASA Wallops Flight Facility.

48

d = 3/4 in.

Nozzle
orientation
centerline

Head-on view

3/4 in.

Side view

Nozzle
orientation
centerline

Along
track

Installation orientation
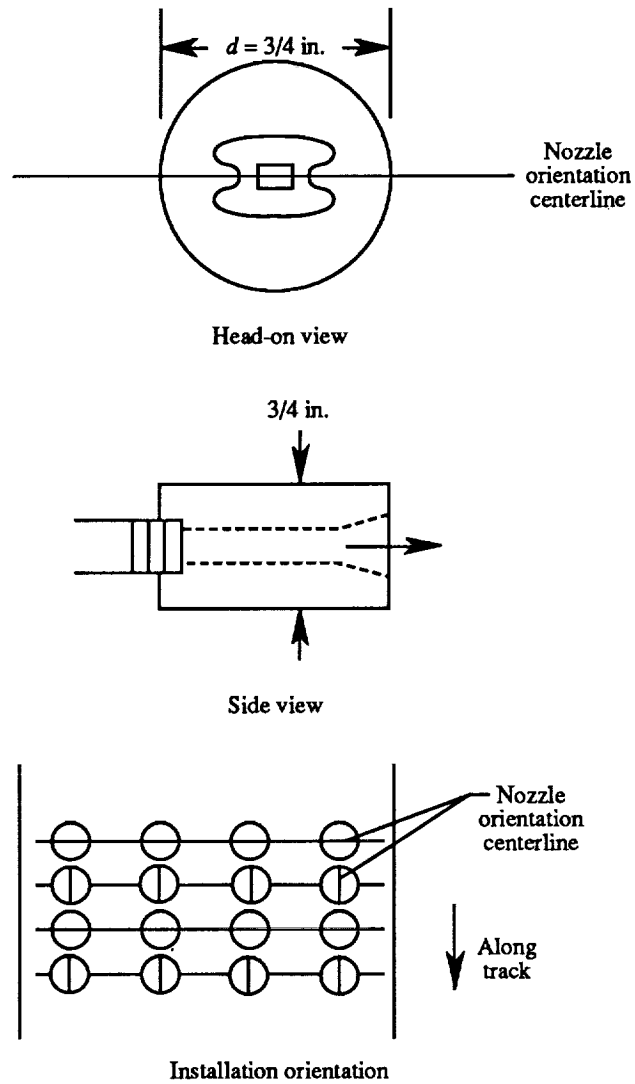
Figure 24. Installation details of 40-in/hr nozzle.
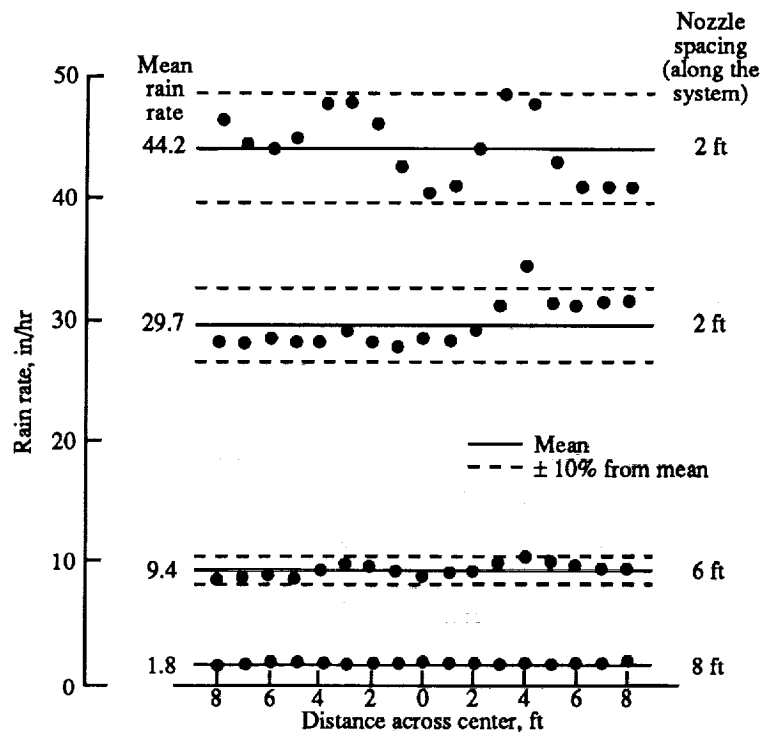
(a) Across the system.
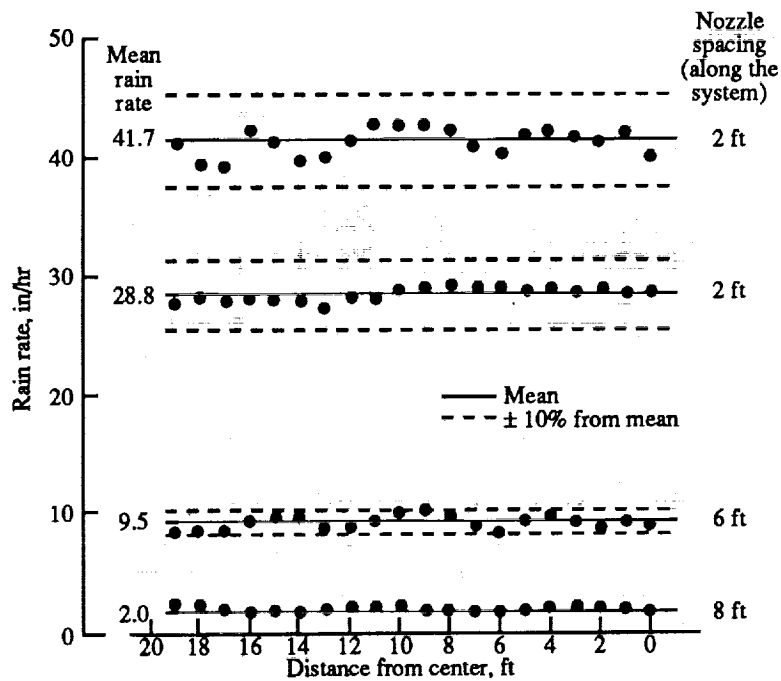
(b) Along the system.

Figure 25. Measured rainfall rates of prototype rain simulation system.

Figure 27. View of piezoelectric device installed on nose of NACA 23015 model fuselage.

L-86-10524

Figure 26. Experimental setup for heavy-rain-effects testing in the Langley 14- by 22-Foot Subsonic Tunnel.

L-87-07697
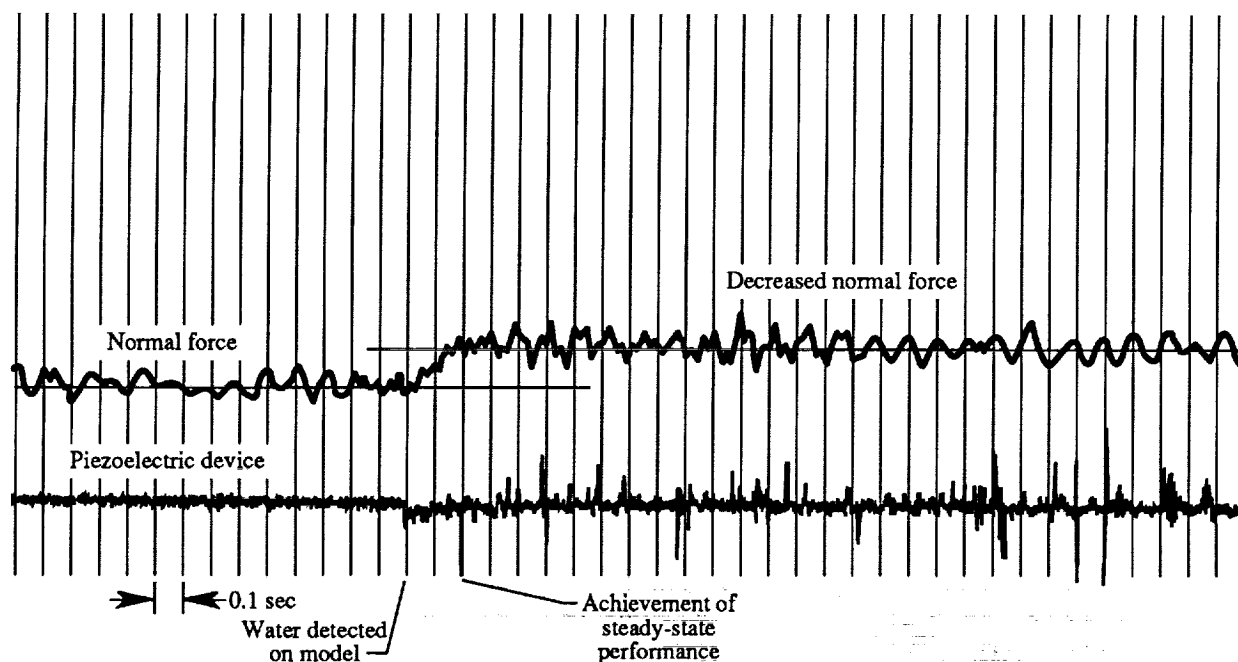
Figure 28. Oscillographic trace showing dynamic response data for NACA 23015 model during transition from dry to wet steady-state conditions for $q = 50$ psf, LWC $= 22$ g/m^3, and $\alpha = 16°$.
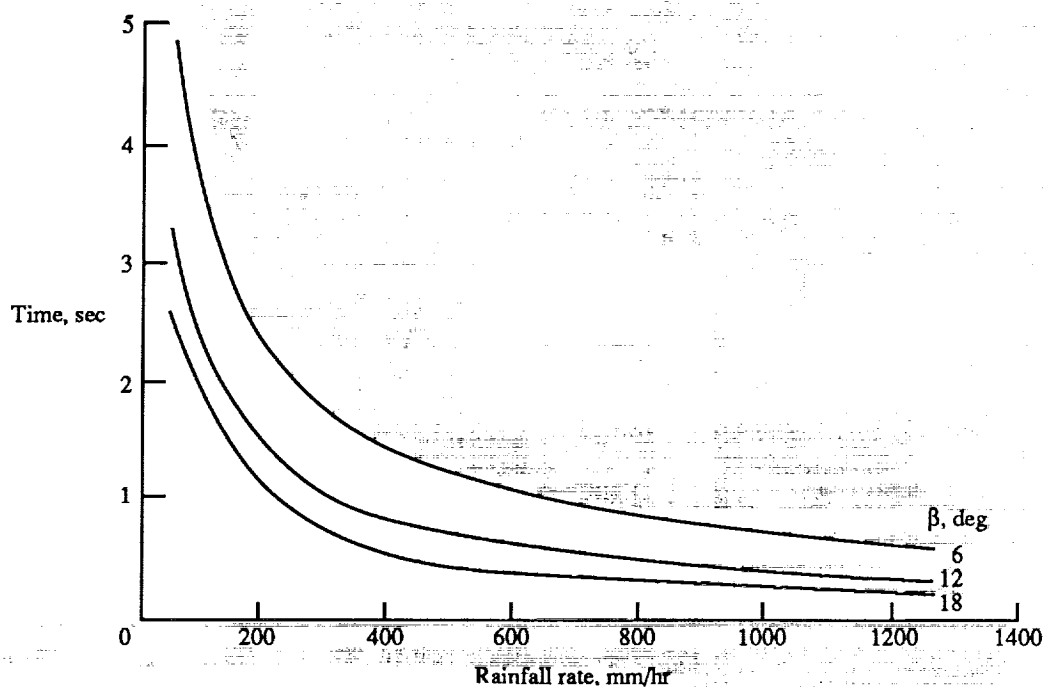
Figure 29. Time needed to develop 90 percent of water film thickness on horizontal flat plate as function of rainfall rate and rain impact angle (β).
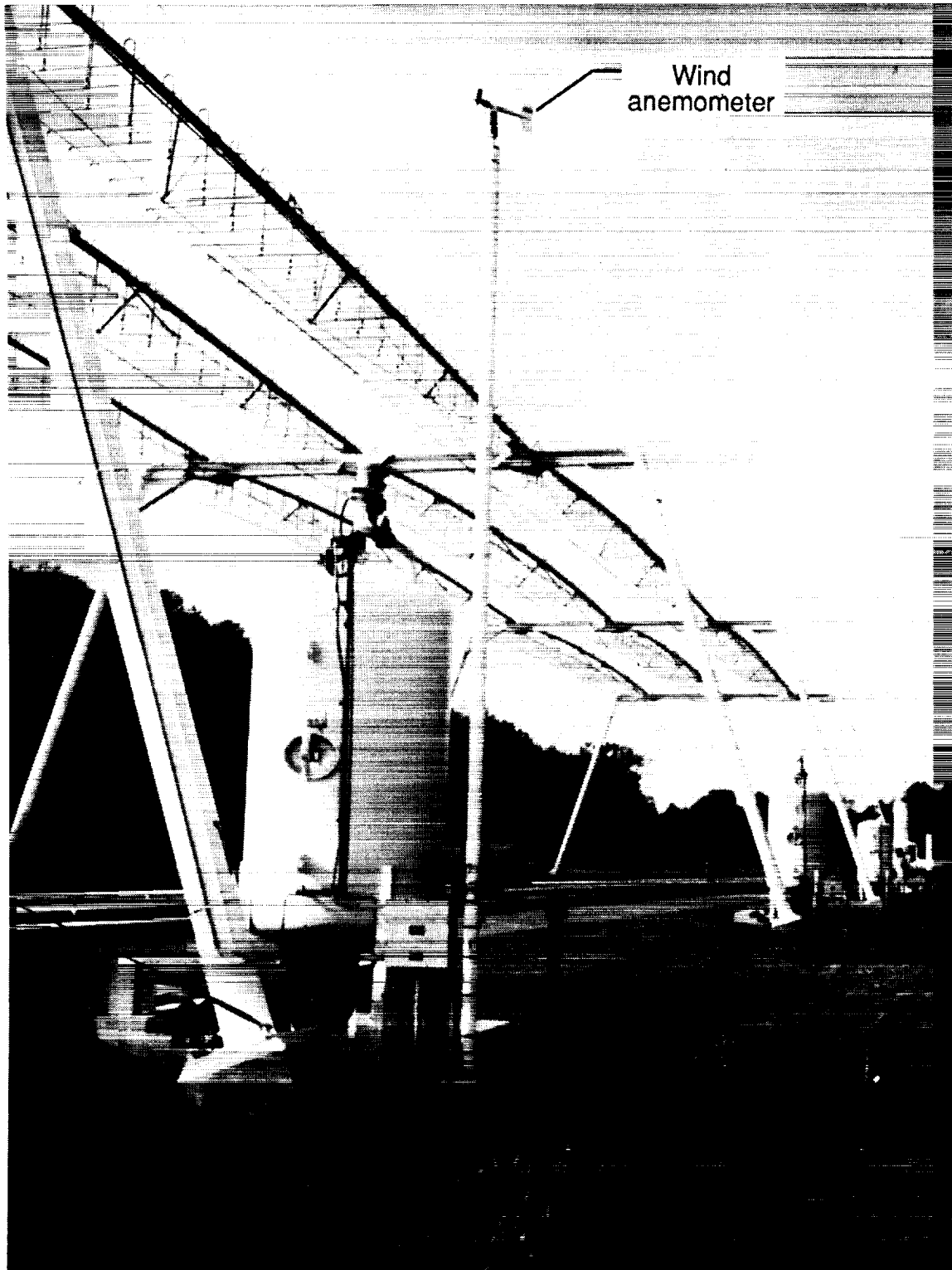
Wind
anemometer

L-89-13513

Figure 30. Photograph of wind anemometer located next to a water-air supply station at the ALDF.
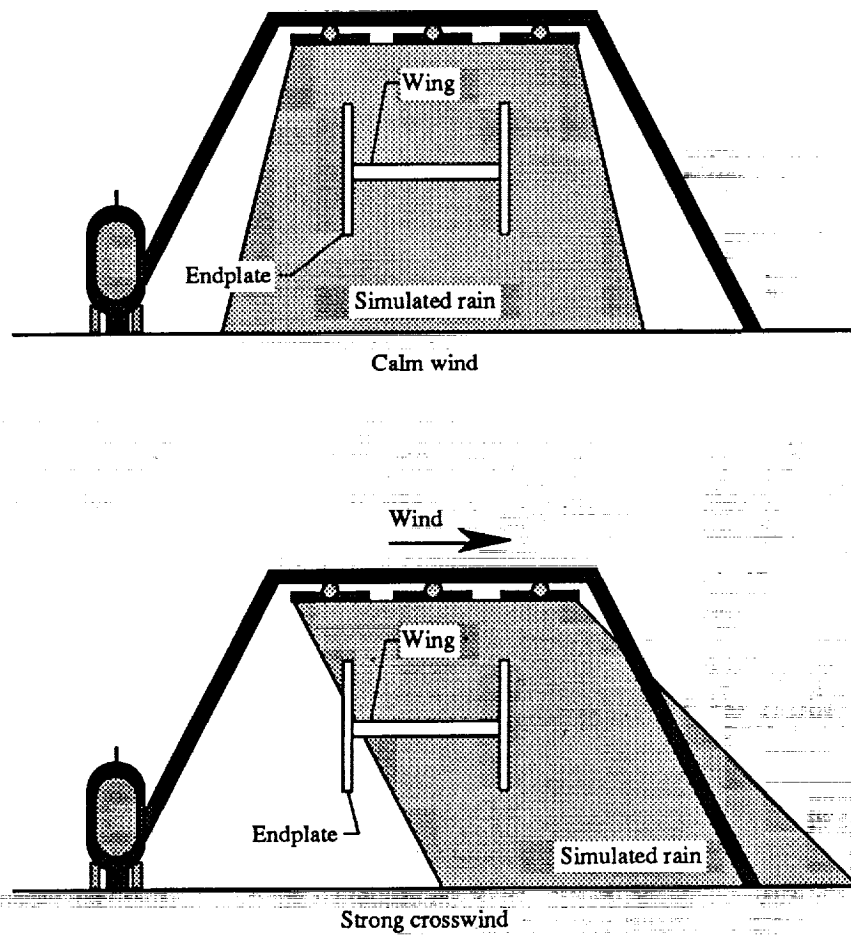
Figure 31. Illustration of effect that crosswinds have on the ALDF RSS.

(a) Without crosswind.

(b) With crosswind.

Figure 32. Photographs of 40-in/hr rain field at the ALDF with and without a crosswind present.

55
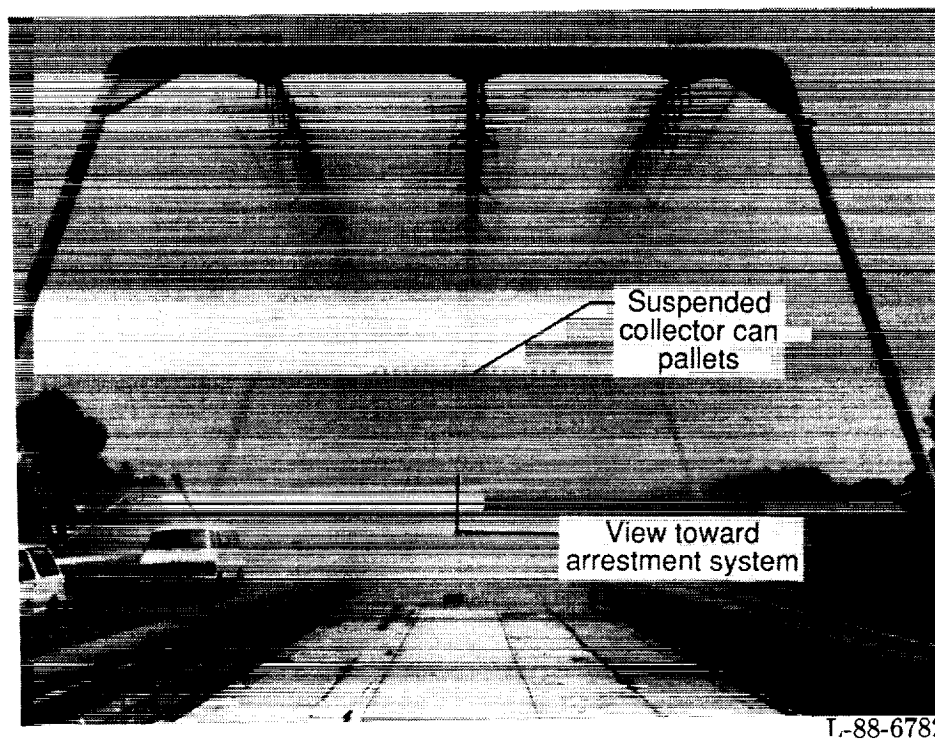
Figure 33. Head-on view of simulated rain field at 40 in/hr during the ALDF RSS calibration process.

Figure 34. Aerial photograph of 40-in/hr simulated rain field.

L-88-3142
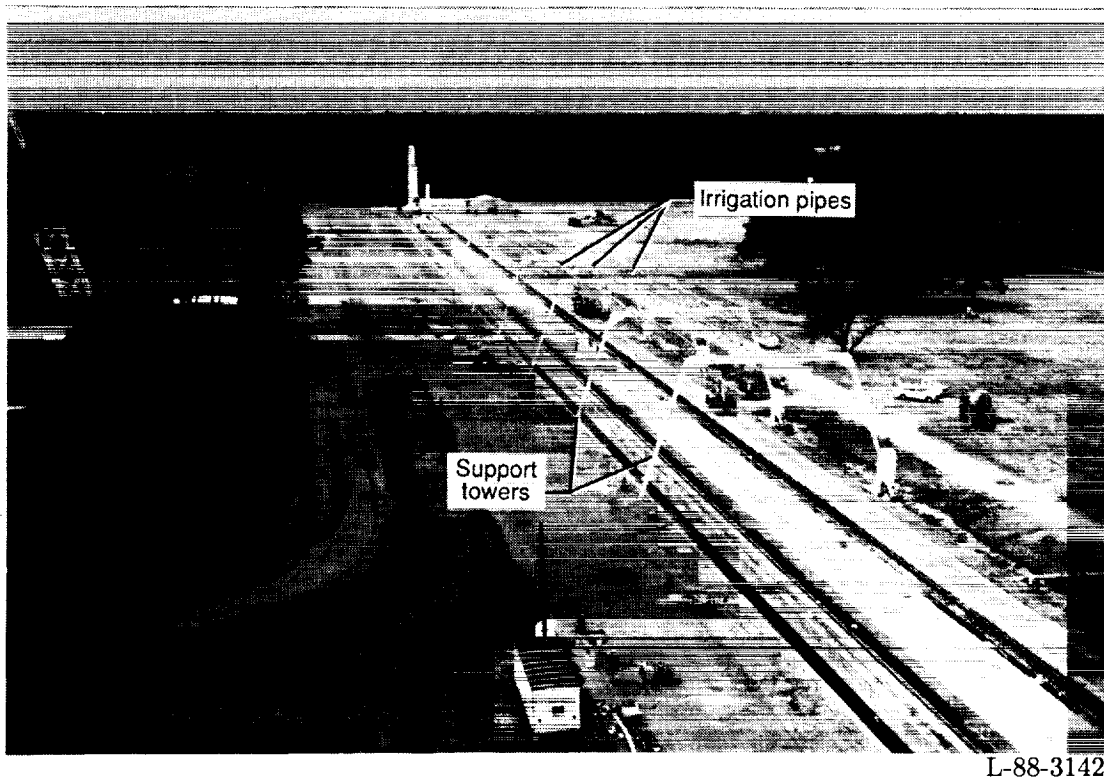
Figure 35. Aerial photograph of the ALDF RSS.

Cross section of
irrigation pipe

Check valve

Regulator

Nozzle

Nozzle

7.5 ft
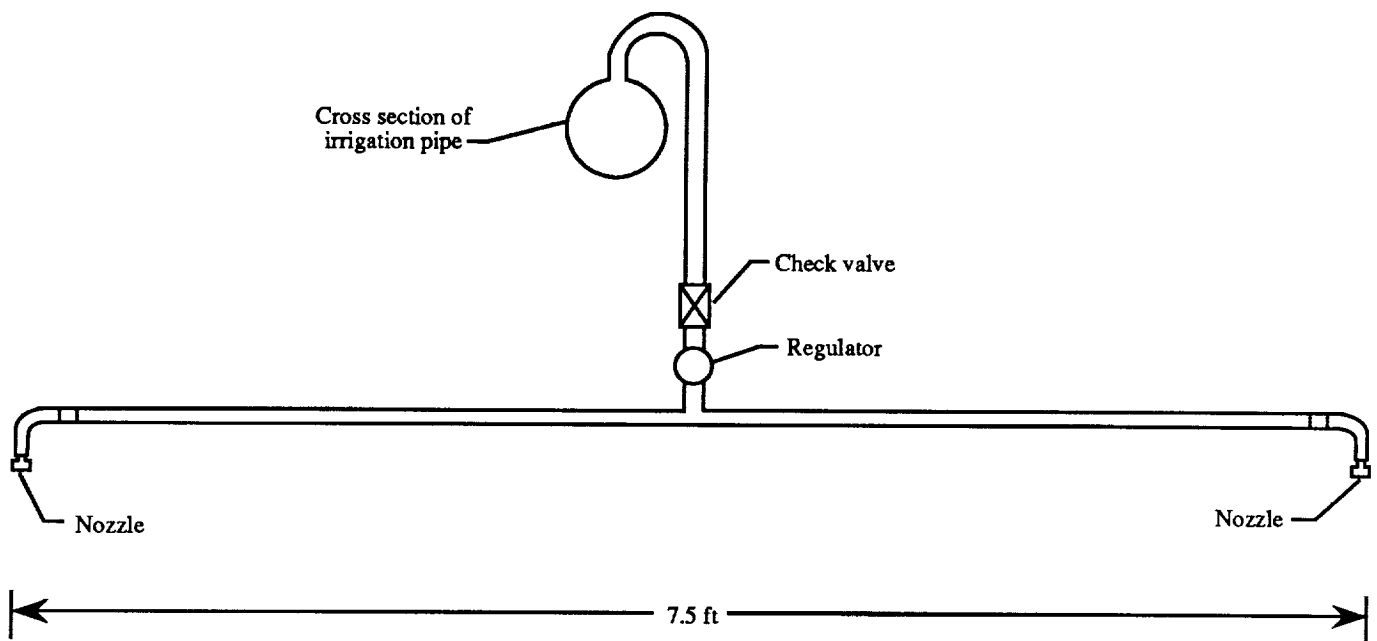
Figure 36. Schematic of drop-pipe assembly.
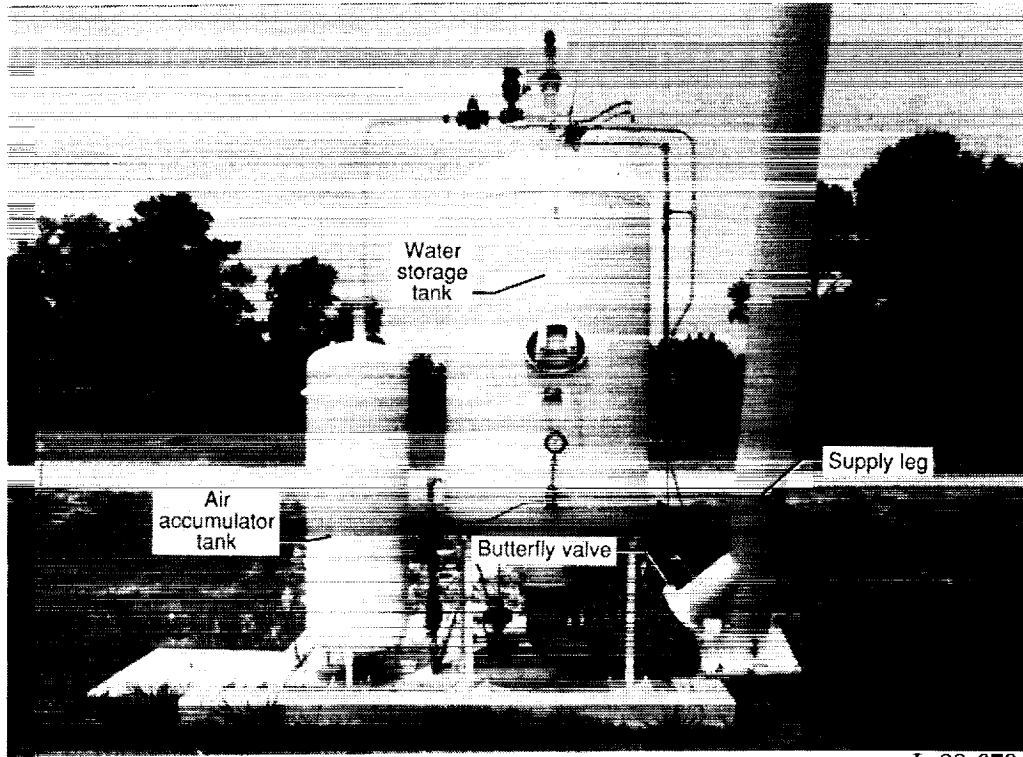
L-88-6794

Figure 37. Photograph of the ALDF RSS water-air supply station.
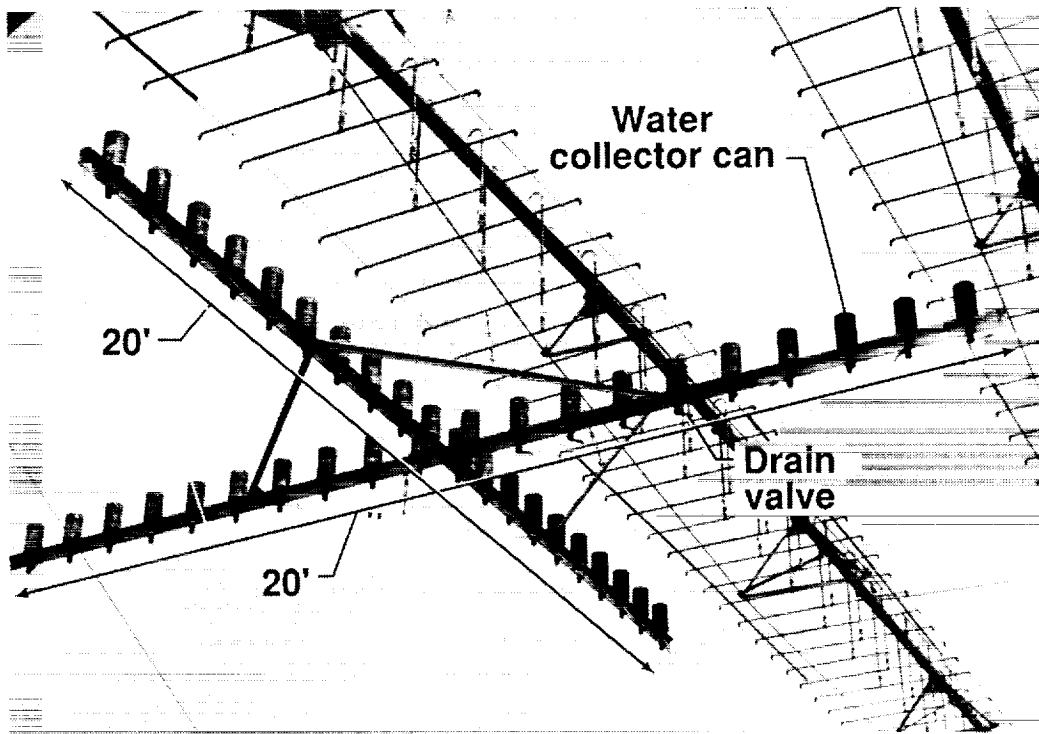
L-88-6788

Figure 38. Photograph of the ALDF RSS calibration using suspended collector can method.

Nozzle pressure: 10 psi Nozzle type: 3/4 in.
Average wind speed: 1.93 mph Nozzle spacing along track: 2 ft
Average direction: 107.5° Nozzle spacing across track: 7.5 ft
Average crosswind: 1.84 mph
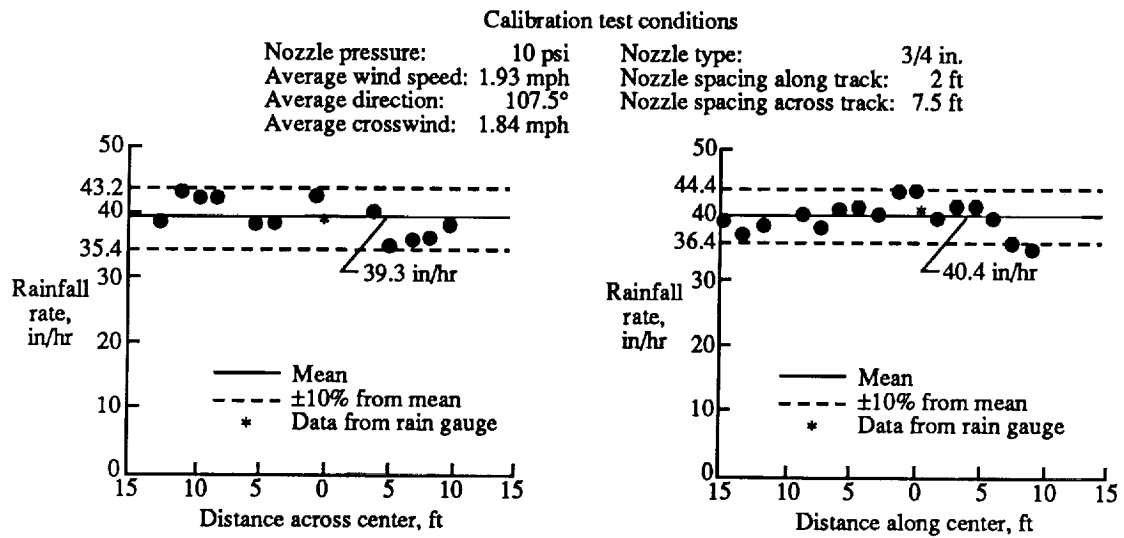
Figure 39. Sample calibration curves across and along the ALDF track for 40-in/hr simulated rain field.

L-88-6793
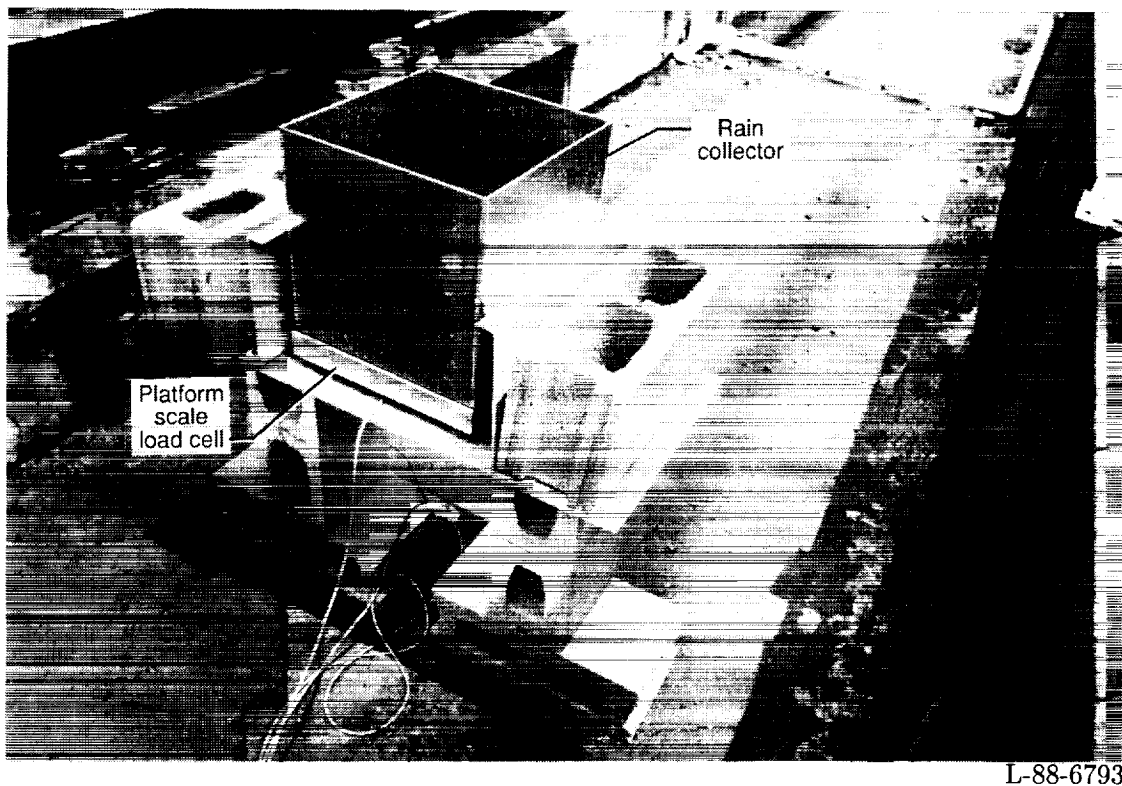
Figure 40. Photograph of weight-measuring rain gauge.

59
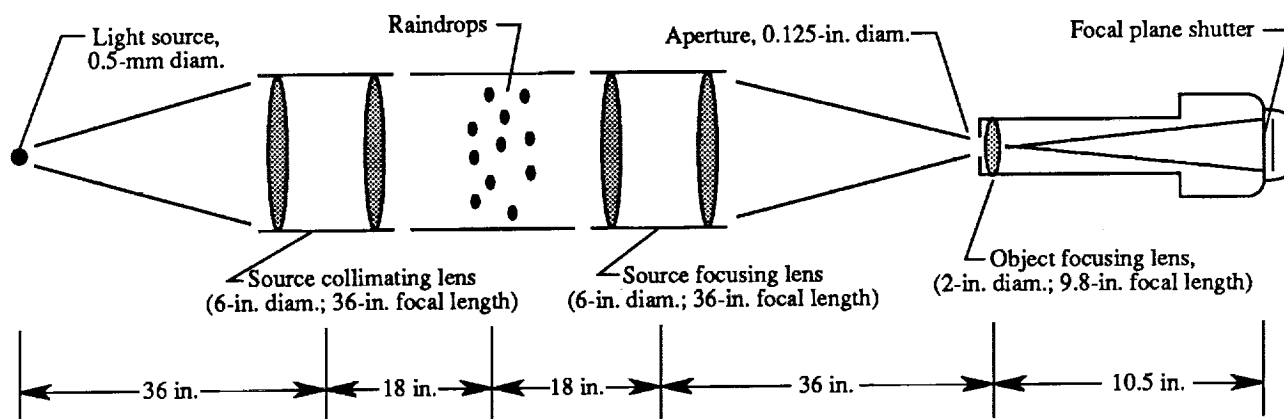
Figure 41. Sketch of shadowgraph photographic method developed to measure raindrop size at the ALDF.
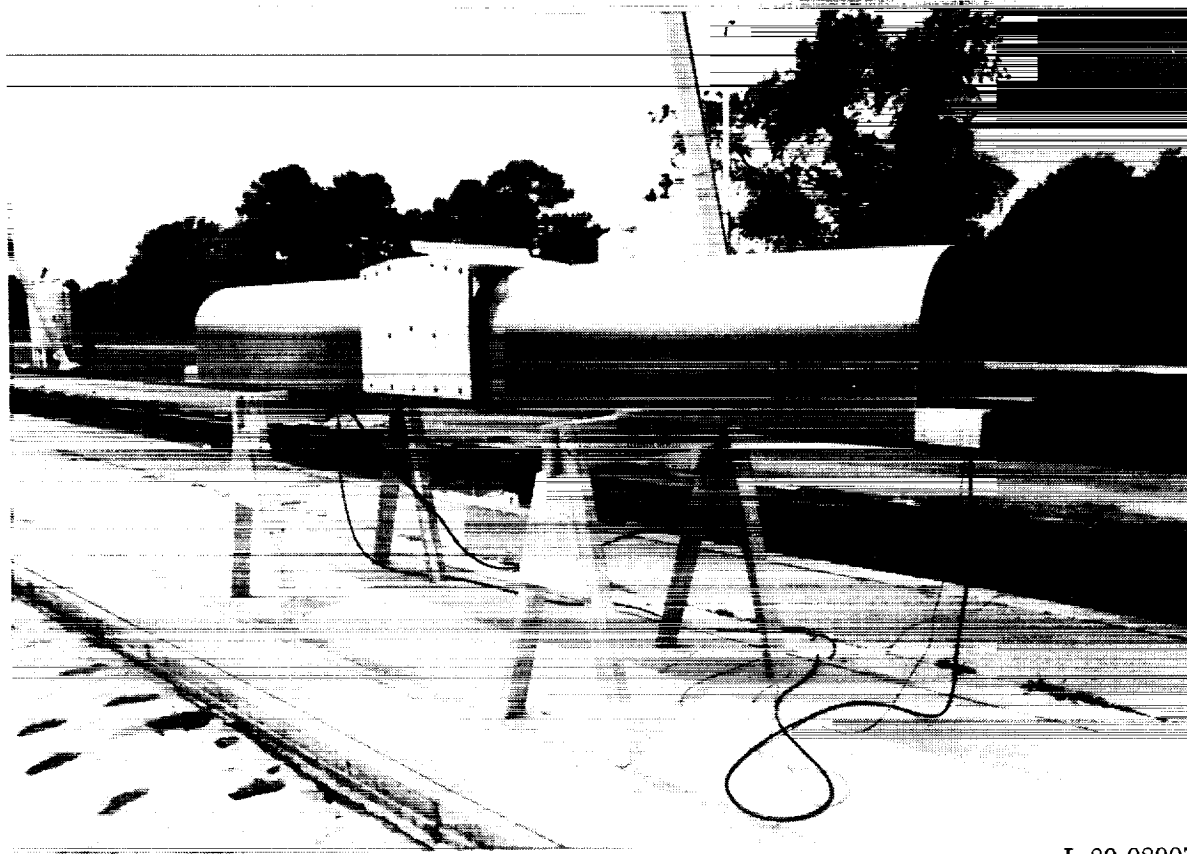
L-89-08907

Figure 42. Photograph of rain shield used to protect shadowgraph hardware.
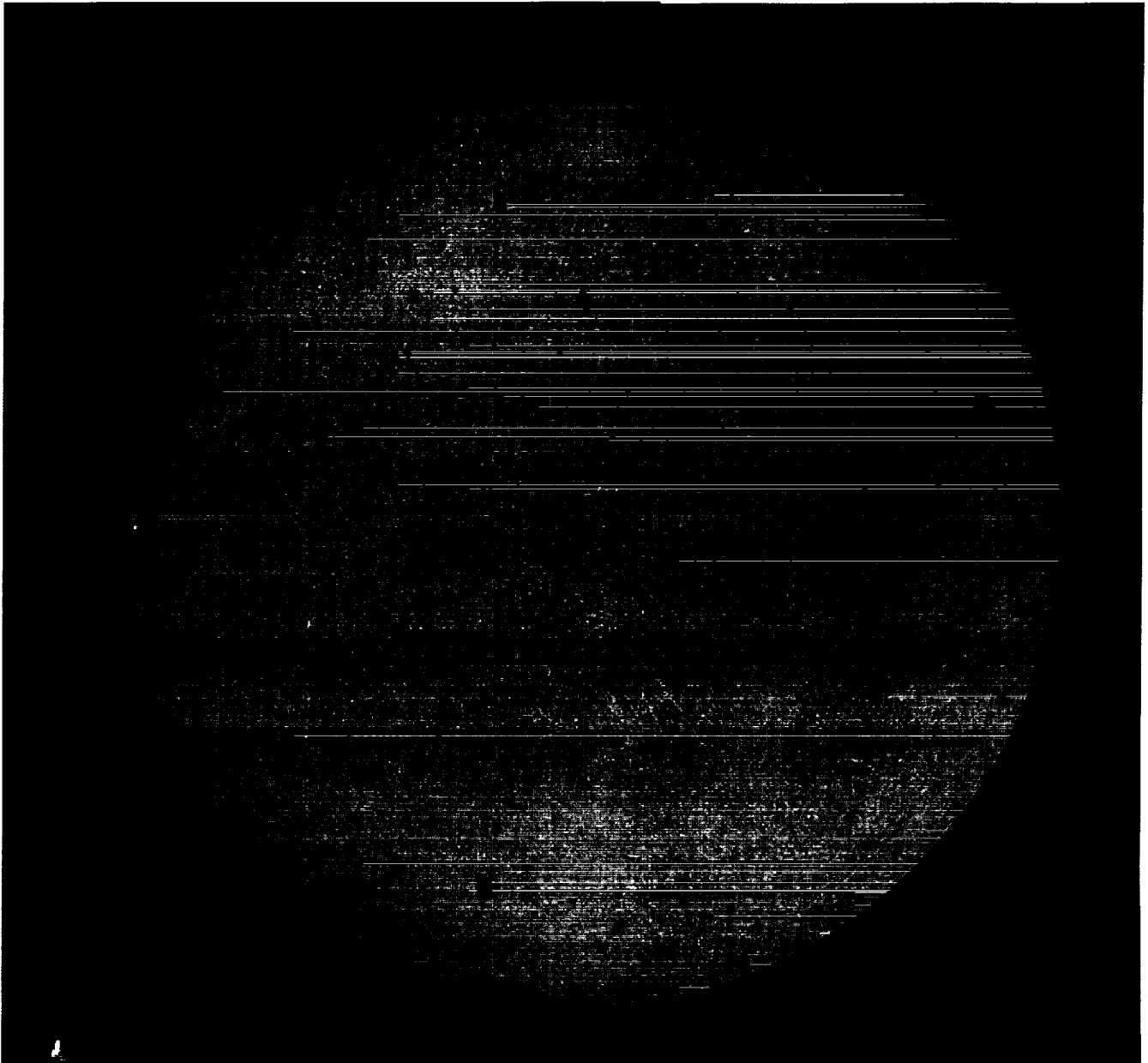
Figure 43. Shadowgraph of the ALDF simulated rain field at 40 in/hr.
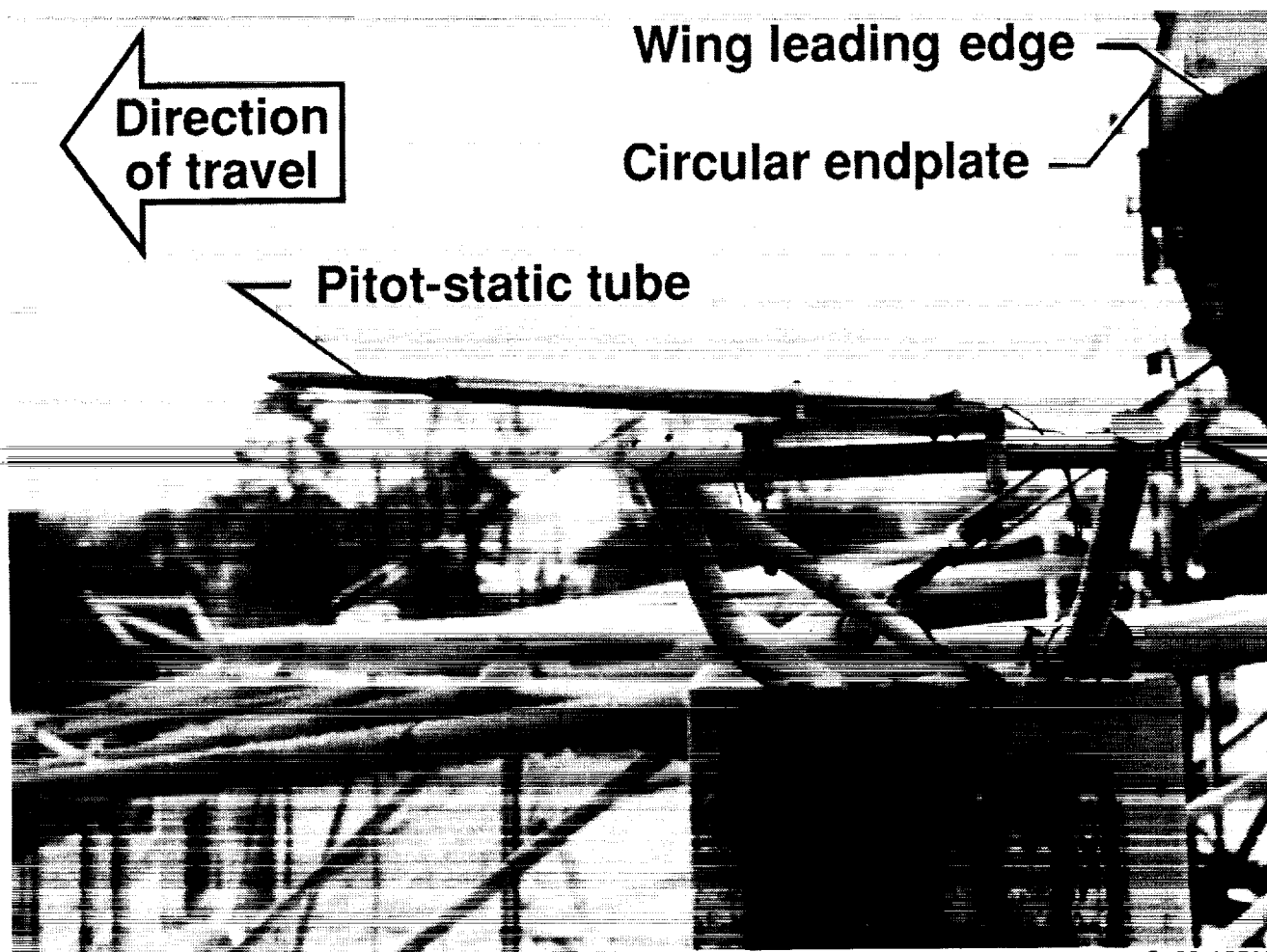
Figure 44. Photograph of standard aircraft Pitot-static tube mounted on a forward extremity of the ALDF carriage.

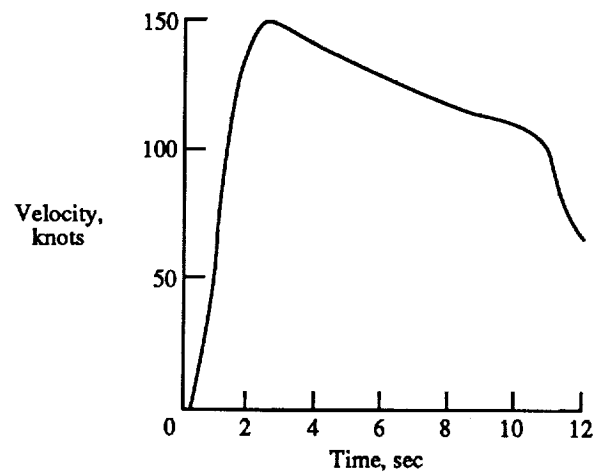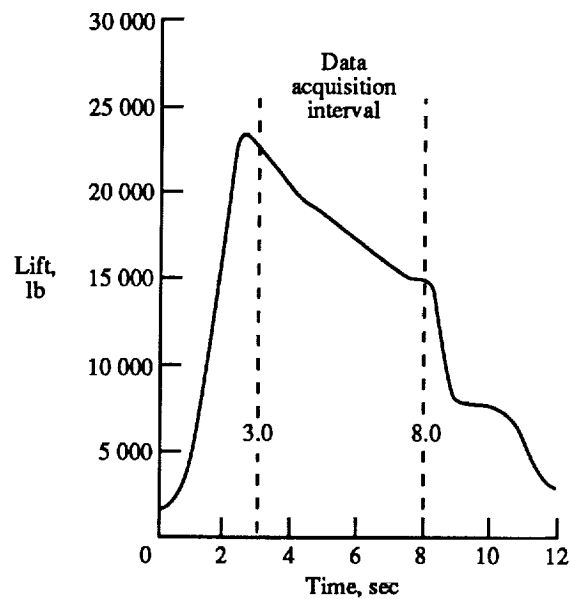Figure 45. Velocity time history of the ALDF carriage based on Pitot-static measurements during calm wind conditions.

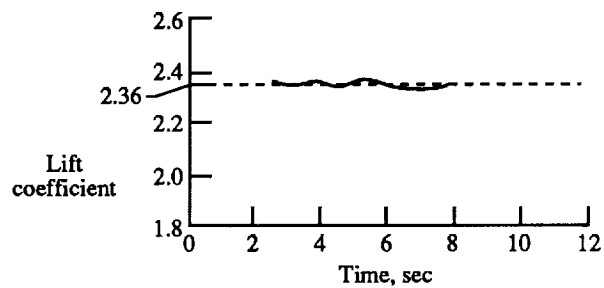Figure 46. Total lift time history during calm wind conditions for landing configuration at $\alpha = 9.5°$.

Figure 47. Lift coefficient time history during calm wind conditions for high-lift configuration at $\alpha = 9.5°$. Average lift coefficient, 2.36.
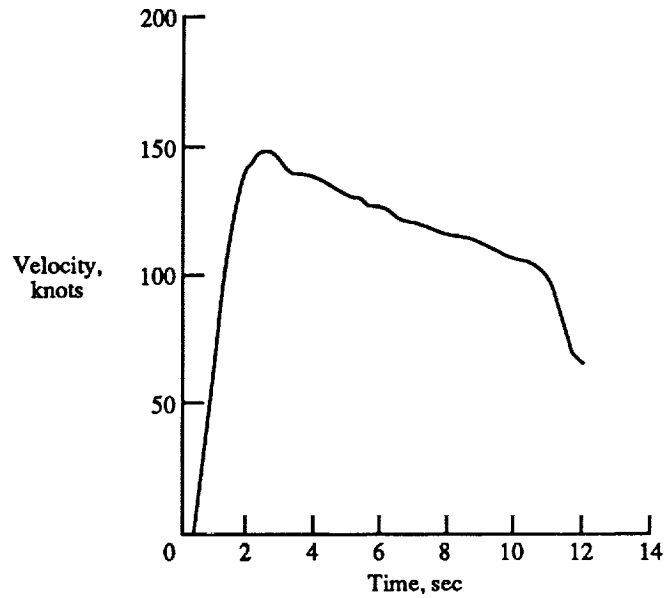
Figure 48. Velocity time history of the ALDF carriage based on Pitot-static readings during crosswind of 5 ft/sec at 280°.
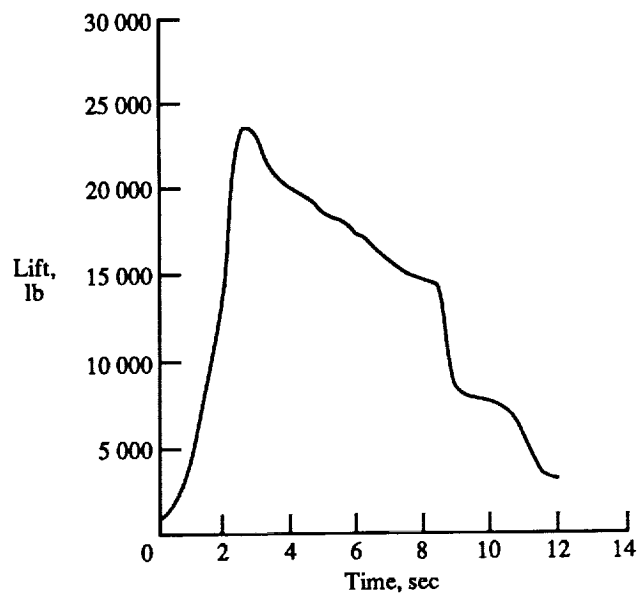

Figure 49. Total lift time history during crosswind of 5 ft/sec at 280° for high-lift configuration at $\alpha = 9.5°$.
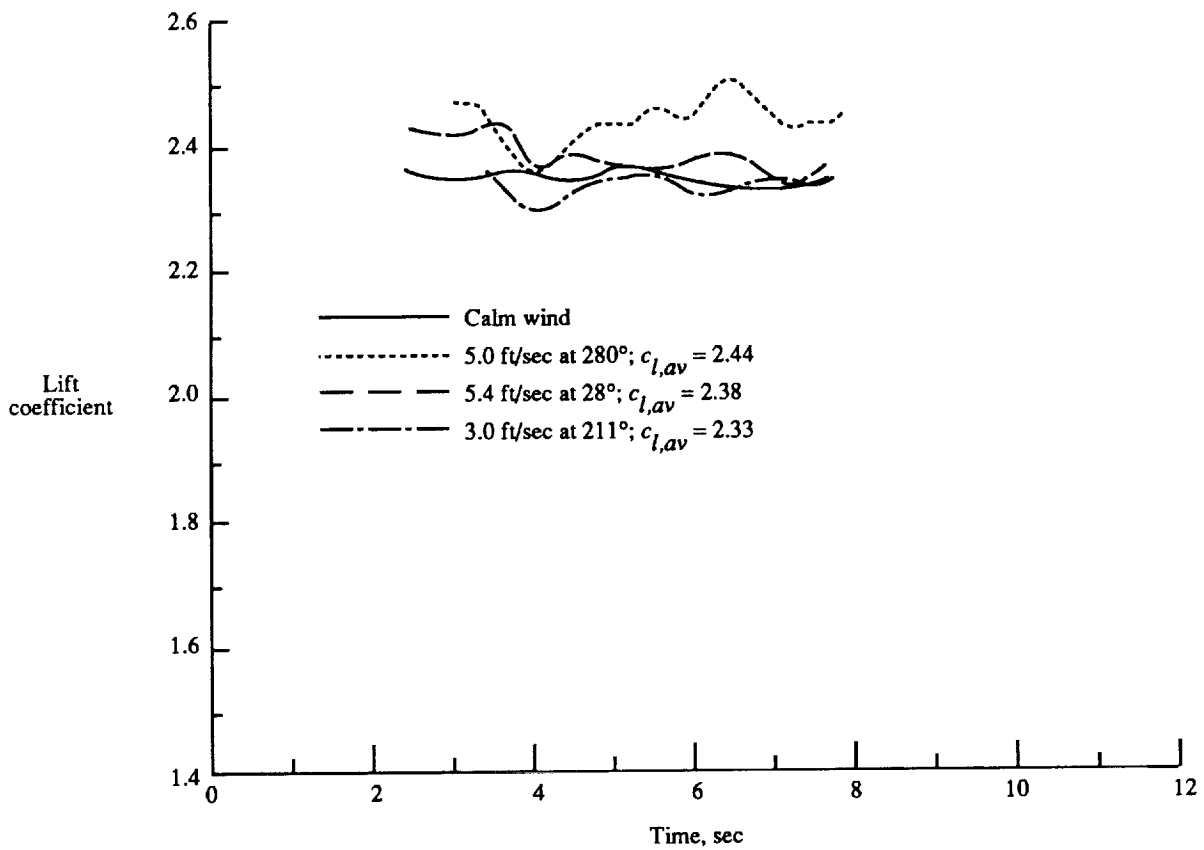
Figure 50. Comparison of lift coefficient time histories for landing configuration at variable crosswind conditions at $\alpha = 9.5°$.

REPORT DOCUMENTATION PAGE

Public reporting burden for this collection of information is estimated to average 1 hour per response, including the time for reviewing instructions, searching existing data sources, gathering and maintaining the data needed, and completing and reviewing the collection of information. Send comments regarding this burden estimate or any other aspect of this collection of information, including suggestions for reducing this burden, to Washington Headquarters Services, Directorate for Information Operations and Reports, 1215 Jefferson Davis Highway, Suite 1204, Arlington, VA 22202-4302, and to the Office of Management and Budget, Paperwork Reduction Project (0704-0188), Washington, DC 20503.

1. AGENCY USE ONLY (Leave blank)	2. REPORT DATE April 1993	3. REPORT TYPE AND DATES COVERED Technical Memorandum

4. TITLE AND SUBTITLE

Development of a Large-Scale, Outdoor, Ground-Based Test Capability for Evaluating the Effect of Rain on Airfoil Lift

5. FUNDING NUMBERS

WU 505-68-01-02

6. AUTHOR(S)

Gaudy M. Bezos and Bryan A. Campbell

7. PERFORMING ORGANIZATION NAME(S) AND ADDRESS(ES)

NASA Langley Research Center
Hampton, VA 23681-0001

8. PERFORMING ORGANIZATION REPORT NUMBER

L-17004

9. SPONSORING/MONITORING AGENCY NAME(S) AND ADDRESS(ES)

National Aeronautics and Space Administration
Washington, DC 20546-0001

10. SPONSORING/MONITORING AGENCY REPORT NUMBER

NASA TM-4420

11. SUPPLEMENTARY NOTES

12a. DISTRIBUTION/AVAILABILITY STATEMENT

Unclassified Unlimited

Subject Category 02

12b. DISTRIBUTION CODE

13. ABSTRACT (Maximum 200 words)

A large-scale, outdoor, ground-based test capability for acquiring aerodynamic data in a simulated rain environment was developed at the Langley Aircraft Landing Dynamics Facility (ALDF) to assess the effect of heavy rain on airfoil performance. The ALDF test carriage was modified to transport a 10-ft-chord NACA 64-210 wing section along a 3000-ft track at full-scale aircraft approach speeds. An overhead rain simulation system was constructed along a 525-ft section of the track with the capability of producing simulated rain fields of 2, 10, 30, and 40 in/hr. This paper describes in detail the facility modifications, the aerodynamic testing and rain simulation capability, the design and calibration of the rain simulation system, and the operational procedures developed to minimize the effect of wind on the simulated rain field and aerodynamic data. The data acquisition and reduction processes are also presented along with sample force data illustrating the environmental effects on data accuracy and repeatability for the "rain-off" test condition.

14. SUBJECT TERMS

Aerodynamics; Heavy rain effects; Large-scale data; Takeoff and landing operations; Transport wing; Rain simulation technique

15. NUMBER OF PAGES

66

16. PRICE CODE

A04

17. SECURITY CLASSIFICATION OF REPORT Unclassified	18. SECURITY CLASSIFICATION OF THIS PAGE Unclassified	19. SECURITY CLASSIFICATION OF ABSTRACT	20. LIMITATION OF ABSTRACT